

Journal of Geophysical Research: Solid Earth

RESEARCH ARTICLE

10.1002/2016JB013080

Key Points:

- New GPS data provide insights on the present-day crustal deformation of the Peruvian Andes
- We describe the kinematics and boundaries of the Peruvian Forearc Sliver and Subandean retro-shortening rates
- We map a highly heterogeneous interseismic coupling pattern of the Nazca megathrust at the scale of the 2200 km of the Peruvian margin

Supporting Information:

- Supporting Information S1
- Table S1

Correspondence to:

J. C. Villegas-Lanza,
juancarlos.villegas@igp.gob.pe

Citation:

Villegas-Lanza, J. C., M. Chlieh, O. Cavalié, H. Tavera, P. Baby, J. Chire-Chira, and J.-M. Nocquet (2016), Active tectonics of Peru: Heterogeneous interseismic coupling along the Nazca megathrust, rigid motion of the Peruvian Sliver, and Subandean shortening accommodation, *J. Geophys. Res. Solid Earth*, 121, doi:10.1002/2016JB013080.

Received 10 APR 2016

Accepted 23 SEP 2016

Accepted article online 24 SEP 2016

Active tectonics of Peru: Heterogeneous interseismic coupling along the Nazca megathrust, rigid motion of the Peruvian Sliver, and Subandean shortening accommodation

J. C. Villegas-Lanza^{1,2}, M. Chlieh², O. Cavalié², H. Tavera¹, P. Baby³, J. Chire-Chira⁴, and J.-M. Nocquet²

¹Instituto Geofísico del Perú, Lima, Peru, ²Géoazur, IRD, Université de Nice Sophia-Antipolis, Observatoire de la Côte d'Azur, CNRS, Valbonne, France, ³Géosciences Environnement Toulouse, Université Paul Sabatier, IRD, CNRS, OMP, Toulouse, France, ⁴Instituto Geográfico Nacional, Lima, Peru

Abstract Over 100 GPS sites measured in 2008–2013 in Peru provide new insights into the present-day crustal deformation of the 2200 km long Peruvian margin. This margin is squeezed between the eastward subduction of the oceanic Nazca Plate at the South America trench axis and the westward continental subduction of the South American Plate beneath the Eastern Cordillera and Subandean orogenic wedge. Continental active faults and GPS data reveal the rigid motion of a Peruvian Forearc Sliver that extends from the oceanic trench axis to the Western-Eastern Cordilleras boundary and moves southeastward at 4–5 mm/yr relative to a stable South America reference frame. GPS data indicate that the Subandean shortening increases southward by 2 to 4 mm/yr. In a Peruvian Sliver reference frame, the residual GPS data indicate that the interseismic coupling along the Nazca megathrust is highly heterogeneous. Coupling in northern Peru is shallow and coincides with the site of previous moderate-sized and shallow tsunami-earthquakes. Deep coupling occurs in central and southern Peru, where repeated large and great megathrust earthquakes have occurred. The strong correlation between highly coupled areas and large ruptures suggests that seismic asperities are persistent features of the megathrust. Creeping segments appear at the extremities of great ruptures and where oceanic fracture zones and ridges enter the subduction zone, suggesting that these subducting structures play a major role in the seismic segmentation of the Peruvian margin. In central Peru, we estimate a recurrence time of 305 ± 40 years to reproduce the great $1746 M_w \sim 8.8$ Lima-Callao earthquake.

1. Introduction

Slip partitioning at an oblique convergent margin is a classical problem that results in a lithospheric sliver detaching from the overriding continental plate [McCaffrey, 2002]. For example, in Sumatra, two thirds of this obliquity is accommodated by the subduction megathrust, with about one third along the great strike-slip fault called the Great Sumatran Fault (GSF); the region between the trench and the GSF is the Sumatran Sliver [Diament et al., 1992]. Along the 7000 km long South American subduction zone, we observe a similar partitioning pattern in South Chile along the Liquiñe-Ofqui Fault [Cembrano et al., 1996; Wang et al., 2007] and in Ecuador and Colombia along the Dolores-Guayaquil Fault zone [Ego et al., 1996]. Another dominant partitioning pattern reported from the Andes is the Subandean shortening in response to the South American Plate subduction below the Subandean regions and the Eastern Cordillera. This shortening is accommodated by the east vergent fold-and-thrust belt of the Eastern Cordillera and Subandean zone. Important Quaternary Subandean shortening rates reaching tens of millimeters per year have been reported in geological and paleomagnetic studies [Dewey and Lamb, 1992; Arriagada et al., 2008]. In contrast, present-day geodetic GPS studies suggest shortening rates no higher than 10 mm/yr [Norabuena et al., 1998; Bevis et al., 2001; Brooks et al., 2011; Métois et al., 2013].

More recently, Nocquet et al. [2014] proposed that the deformation in the Northern Andes is controlled by the diverging motion of two rigid continental slivers, the previously known North Andean Sliver that covers Ecuador and Colombia north of the Gulf of Guayaquil and a newly found Inca Sliver that encompasses southernmost Ecuador, Peru, and Bolivia from the trench axis to the Subandean fold-and-thrust belt. Based on a direct analysis of a subset of 28 GPS measurements showing a coherent motion in a stable South America (SSA) reference frame, Nocquet et al. [2014] proposed an Euler pole for the Inca Sliver relative to SSA (Inca/SSA; Table 2) located on the Caribbean Plate at 63.76°W and 22.47°N with an angular velocity of $0.092^\circ/\text{Myr}$. This pole predicted a south-eastward motion of the Inca Sliver at about 5 mm/yr relative to

SSA, but southern and eastern boundaries of the Inca Sliver are uncertain. In particular, *Nocquet et al.* [2014] did not test if their data were compatible with a central Andes microplate thought to span much of the Altiplano of southern Peru, northern Chile, and western Bolivia [*Bevis et al.*, 2001; *Bird*, 2003]. *Chlieh et al.* [2011] noticed an asymmetry in the mode of Subandean shortening between southern Peru/northern Bolivia, where 4 mm/yr of shortening is suggested by the GPS data, and northern Chile/southern Bolivia, where 10 mm/yr of shortening is needed to explain the large GPS motion there. This asymmetry suggests that the central Andes could potentially not be considered to be as a single rigid microplate.

Great ($M_w > 8.5$) megathrust earthquakes have occurred along the Peruvian subduction zone. The last ones were the 1746 ($M_w = 8.8$) Lima-Callao earthquake in central Peru that ruptured about a 550 km long portion of the subduction zone and the 1868 ($M_w = 8.8$) south Peru earthquake that ruptured 450 km further south (Figure 1) [*Dorbath et al.*, 1990]. The great 1746 Lima-Callao earthquake shares characteristics similar to the recent 2010 ($M_w = 8.8$) Maule earthquake, which also broke a segment of about 550 km long (Figure 1), triggering a destructive tsunami. Since these ruptures, the Peruvian megathrust has experienced frequent large ($M_w > 7.5$) earthquakes that ruptured only fractions of the great 1746 and 1868 ruptures. For instance, the 2001 ($M_w = 8.4$) Arequipa event ruptured about two thirds of the 1868 rupture, leaving a seismic gap between Tacna and Arica in southern Peru. In central Peru, the 2007 $M_w = 8.0$ Pisco earthquake ruptured about one quarter of the 1746 rupture. The 2007 Pisco earthquake was the last of a sequence of $M_w \sim 8.0$ events that occurred in 1940, 1966, 1974, and 2007. It is worth noting that even if the accumulated rupture area of these four large earthquakes roughly overlaps the 1746 rupture area, the 1940–2007 seismic moment is half or less than the 1746 seismic moment, suggesting a much higher slip during the great 1746 earthquake.

Previous interseismic GPS studies in Peru have reported a high level of frictional coupling along the subduction interface from the trench (or close to it) down to a depth of about 50 km [*Norabuena et al.*, 1998; *Bevis et al.*, 2001; *Gagnon et al.*, 2005; *Chlieh et al.*, 2011]. *Chlieh et al.* [2011] proposed a heterogeneous coupling model with fully locked asperities separated by creeping segments. Based on the limited GPS data for central Peru, they estimated that a $M_w > 8.5$ subduction earthquake is overdue for central Peru. By contrast, *Nocquet et al.* [2014] found an ~1000 km long creeping segment in northern Peru and southern Ecuador, suggesting that the possibility of a $M_w > 9.0$ earthquake in northern Peru and southern Ecuador may be less likely. So far, many homogeneous and heterogeneous interseismic coupling models have been proposed for different portions of the 2200 km long Peruvian megathrust [*Norabuena et al.*, 1998; *Bevis et al.*, 2001; *Kendrick et al.*, 2001; *Gagnon et al.*, 2005; *Chlieh et al.*, 2011; *Nocquet et al.*, 2014]. However, there is no uniform solution at the scale of the entire Peruvian subduction zone, which we propose to do here.

In this paper, we revisit the slip partitioning of the Peruvian margin, and include new geodetic constraints on the present-day velocities along the coast, in the Western and Eastern Cordilleras, and in the Subandean regions. We thus provide new constraints on the Subandean shortening rate and a new definition of the Peruvian Forearc Sliver. Then, using this new Peruvian Forearc Sliver as a reference frame, we explore a wide range of interseismic coupling models based on the residual interseismic GPS gradients. We finally propose a large-scale heterogeneous interseismic coupling model from the Gulf of Guayaquil at a latitude of ~3°S to the Arica bend at a latitude of ~19°S. To achieve that, we use a large number of updated geophysical observations from (1) a 2008–2013 GPS velocity field that includes 103 sites distributed over the Andes of Peru and covering coastal regions, the Andes Cordilleras, and the Subandean regions. In addition to the 38 GPS sites in Peru that were used in *Nocquet et al.* [2014], we include 36 new permanent GPS stations and 15 new campaign sites across three profiles in the north and central Andes of Peru. We also use (2) updated historical and recent seismological data from seismic and tsunami catalogues and paleoseismic studies, (3) active faults from public databases, (4) focal mechanisms from the global centroid moment tensor catalogue (gCMT), and (5) the corrected Slab1.0 model [*Hayes et al.*, 2012] for the subduction megathrust geometry.

2. Seismotectonic Setting

2.1. Updated Catalogue of Historical Large Megathrust Earthquakes in Peru

The history of its seismicity, together with the morphological features of the subducting Nazca Plate, have led previous authors to divide the Peruvian subduction zone into three major segments (Figures 1b and 1c) [*Silgado*, 1978; *Dorbath et al.*, 1990; *Nishenko*, 1991; *Tavera and Buforn*, 1998; *Bilek*, 2010]:

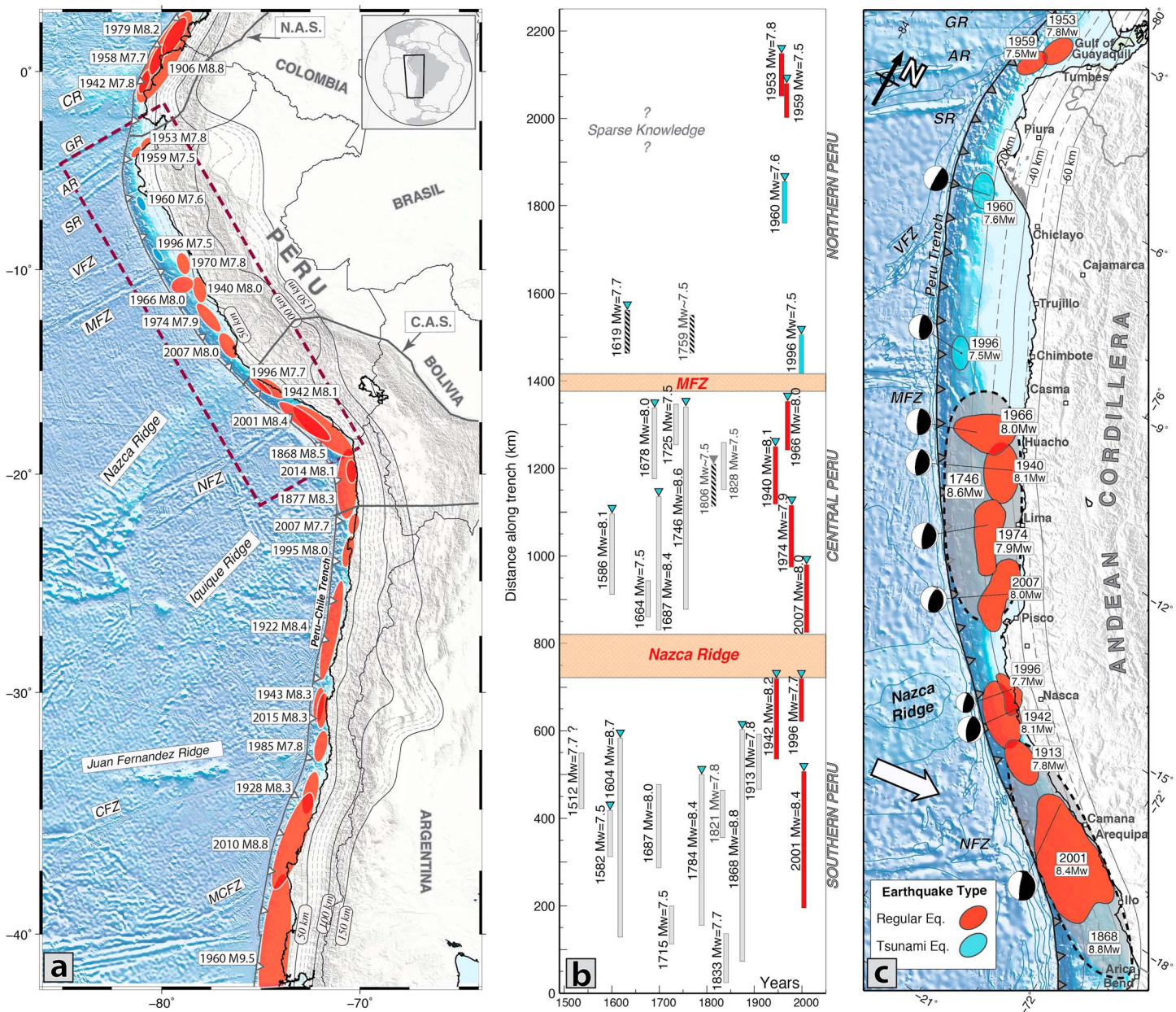


Figure 1. (a) Seismotectonic setting of the South American subduction zone. The red ellipses indicate the approximate rupture areas of large subduction earthquakes ($M \geq 7.5$) between 1868 and 2015 [Silgado, 1978; Beck and Ruff, 1989; Dorbath et al., 1990; Beck et al., 1998]. The blue ellipses indicate the locations of moderate tsunami-earthquakes [Pelayo and Wiens, 1990; Ihmle et al., 1998]. The bathymetry from GEBCO30s highlights the main tectonic structures of the subducting Nazca Plate, which are from north to south: Carrión Ridge (CR), Grialva Ridge (GR), Alvarado Ridge (AR), Sarmiento Ridge (SR), Virú Fracture Zone (VFZ), Mendaña Fracture Zone (MFZ), Nazca Ridge (NR), Nazca Fracture Zone (NFZ), Iquique Ridge, Juan Fernandez Ridge, Challenger Fracture Zone (CFZ), and Mocha Fracture Zone (MCFZ). The white arrow indicates the convergence of the Nazca Plate relative to the stable South America (SSA) reference frame [Kendrick et al., 2003]. The slab geometry isodepth contours are reported every 50 km (solid lines) and 10 km (dashed lines), based on the Slab1.0 model [Hayes et al., 2012]. The dashed rectangle corresponds to Figures 1b and 1c. The N.A.S. and C.A.S. labels indicate the North Andean and the Central Andes Slivers [Bird, 2003], respectively. (b) Temporal and spatial distributions of large subduction earthquakes with $M_w \geq 7.5$ that occurred in Peru since the sixteenth century. The rupture extent values (in km) of historical (gray) and recent (red) megathrust earthquakes along the Peruvian margin are shown as a function of time (in years). A triangle indicates if a tsunami was associated with the event. The orange bands denote the entrance of the NR and the MFZ delimiting the northern, central, and southern Peru subduction segments. The rupture lengths were taken from its corresponding published slip models [Silgado, 1978; Beck and Ruff, 1989; Dorbath et al., 1990; Pelayo and Wiens, 1990; Ihmle et al., 1998; Giovanni et al., 2002; Salichon et al., 2003; Pritchard et al., 2007; Bilek, 2010; Delouis et al., 2010; Moreno et al., 2010; Schurr et al., 2014], and for historical earthquakes, we estimated its approximated lengths using scaling law relationships [Wells and Coppersmith, 1994]. (c) A map of the rupture areas of large subduction earthquakes that occurred in the twentieth century [Silgado, 1978; Beck and Ruff, 1989; Dorbath et al., 1990; Ihmle et al., 1998; Giovanni et al., 2002; Sladen et al., 2010; Chlieh et al., 2011], with their associated gCMT focal mechanisms. In northern Peru, the 1960 ($M_w = 7.6$) Piura earthquake and the 1996 ($M_w = 7.5$) Chimbote earthquake, which are shown by cyan-colored polygons, were identified as tsunami-earthquake events [Pelayo and Wiens, 1990; Ihmle et al., 1998; Bilek, 2010].

1. The northern Peru segment, extending from the Gulf of Guayaquil at latitude 3°S to latitude 10°S.
2. The central Peru segment, bounded by the Mendaña fracture zone (10°S) to the north and the Nazca Ridge (~15°S) to the south.
3. The southern Peru segment, which extends from the Nazca Ridge to the Arica bend (19°S) adjacent to the northern Chile segment.

The southern and central Peru segments are characterized by recurrent great ($M \geq 8.5$) and large ($M \geq 7.5$) megathrust earthquakes with characteristic recurrence times of about 100–300 years [Kelleher, 1972; Dorbath *et al.*, 1990]. In contrast, the northern Peru segment is characterized by the absence of great earthquakes and the sparse occurrence of moderate- to large-magnitude earthquakes able to trigger local tsunamis. The largest subduction earthquakes reported so far for northern Peru are the 1619 ($M_w = \sim 7.7$), 1953 ($M_w = 7.8$), 1959 ($M_w = 7.5$), 1960 ($M_w = 7.6$), and 1996 ($M_w = 7.5$) events (Figures 1b and 1c). The latter two events had all of the characteristics of tsunami-earthquakes: a slow rupture velocity, long source time duration, and local tsunamis significantly greater than expected for their initial M_s values [Pelayo and Wiens, 1990; Ihmle *et al.*, 1998; Bourgeois *et al.*, 1999]. However, we notice that for the 1953 and 1959 events, the tsunami catalogues (National Geophysical Data Center; <http://www.ngdc.noaa.gov>) [Soloviev and Go, 1975; Lockridge, 1985; Espinoza, 1992; Ioualalen *et al.*, 2014] report local tsunamis with runup heights greater than 1 m near Tumbes and the surrounding areas, including southern Ecuador (latitude 3°S to 4°S), indicating that they were, most likely, shallow events. It is worth noting that those two events were not considered in the previous compilations of large earthquakes for Peru [Dorbath *et al.*, 1990; Bilek, 2010]. Here we include these latest events and provide an updated catalogue of the large megathrust earthquakes in Peru (Figure 1b and Table S1 in the supporting information).

Figure 1b shows the updated temporal distribution of historical and recent large ($M \geq 7.5$) subduction earthquakes, together with their estimated rupture areas along the whole Peruvian subduction zone. Although the 1970 ($M_w = 7.8$) Ancash earthquake that triggered a major landslide is by far the most catastrophic event in Peru (with a death toll over 70,000 people), it was not included in our compilation as a subduction megathrust event because it was a normal fault-type event that occurred within the downgoing Nazca Plate [Abe, 1972]. Figure 1c shows that the northern segment is much less seismically active than the central and southern segments. However, the occurrence of moderate to large earthquakes indicates that some areas of the megathrust are accumulating elastic stresses. Although Nocquet *et al.* [2014] showed that a 1000 km creeping segment in the northern Andes is predominantly creeping, significant coupling could also accumulate at the shallowest 20 km depth portion of the megathrust interface, where GPS data provide low resolution.

2.2. Active Faults of the Peruvian Andes

The main geomorphological features of the Peruvian margin are from west to east: the trench axis, the coastal plains and Cordillera, the Western Cordillera, the Altiplano Plateau in the Southern Peru segment, the fold and thrust belt of the Eastern Cordillera, and the Subandean foreland basin system [Dalmayrac, 1978; Suarez *et al.*, 1983; Mégard, 1984; Eude *et al.*, 2015]. Figure 2 shows the main active faults from recent geological compilations [Macharé *et al.*, 2003; Veloza *et al.*, 2011] (<http://neotec-opendata.com>) together with the focal mechanism of significant earthquakes ($M_w \geq 5.5$) [Suarez *et al.*, 1983; Devlin *et al.*, 2012; Ekström *et al.*, 2012]. Active reverse faulting is found all along the Subandean fold and thrust belts. The shortening direction varies from east in northern Peru to NNE in southern Peru. Structural balanced cross sections combined with the deformation ages and paleomagnetic reconstructions [Baby *et al.*, 1997; Oncken *et al.*, 2006; Arriagada *et al.*, 2008; Eude *et al.*, 2015] suggest that since the Middle Neogene, the Eastern Cordillera and Subandean foreland basins have been very active by accommodating tens to hundreds of kilometers of crustal shortening. In Peru the total horizontal shortening of the Eastern Cordillera and Subandean thrust system varies from 70 km in the north (Huallaga-Marañon foreland basin system) [Eude *et al.*, 2015] to 47 km in the south (Madre de Dios foreland basin system). Within the Andes, a complex pattern of deformation is observed, with a combination of reverse, normal, and strike-slip faults. A segmented active fault system appears along the boundary between the Western Cordillera and Eastern Cordillera (Figure 2). This boundary roughly follows the transpressional Marañon Fault System in northern Peru, the Chonta Fault System in central Peru, and the Urcos-Ayaviri-Copacabana-Coniri Fault System in southern Peru. These fault systems are generally described as left-lateral strike-slip faults [Sempere *et al.*, 2004; Rodriguez Mejia, 2008; Scherrenberg *et al.*,

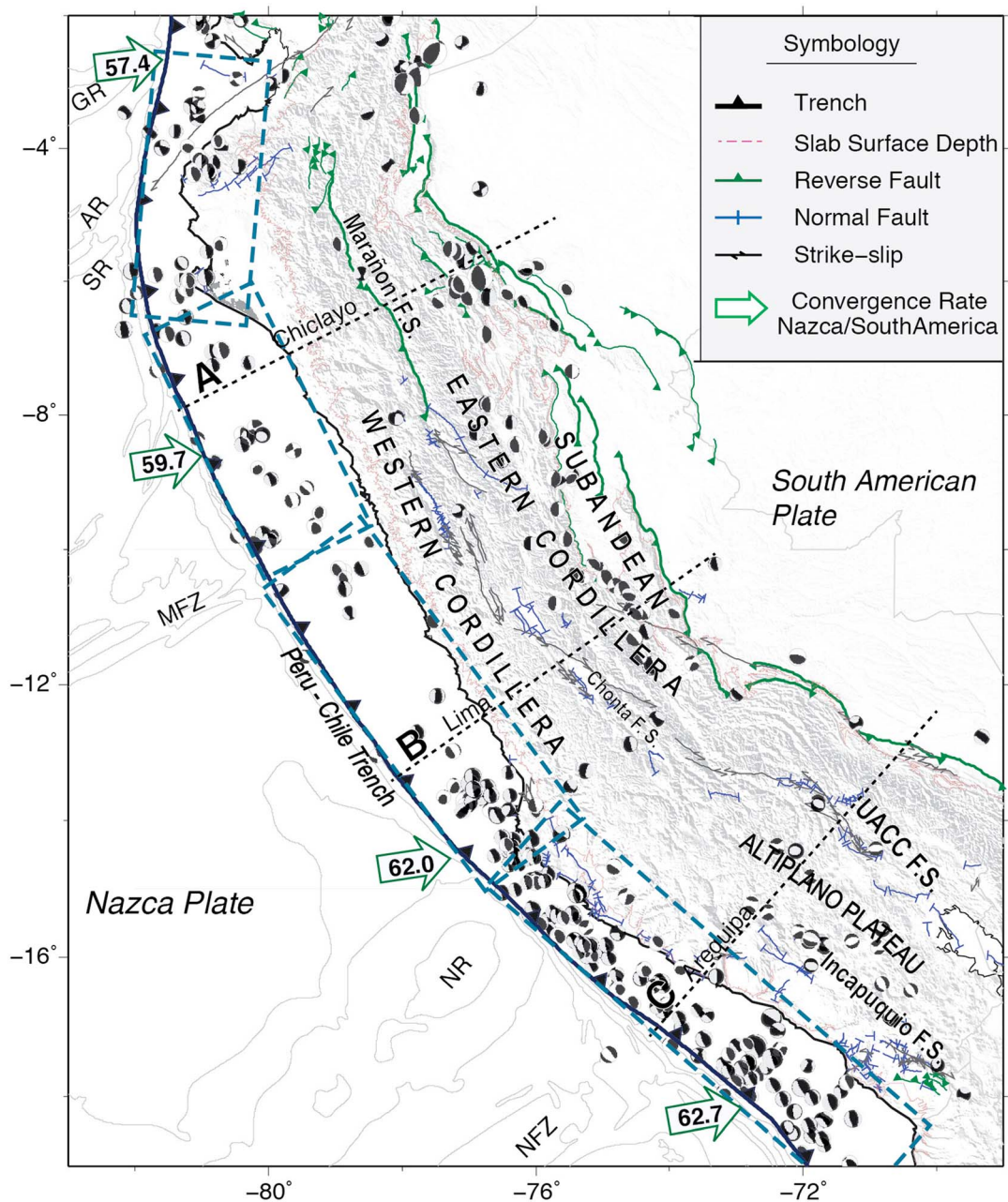


Figure 2. Neotectonic setting of the Peruvian margin. The arrows indicate the convergence of the Nazca Plate (in mm/yr) relative to the SSA as predicted by the Euler pole of Kendrick *et al.* [2003]. The main quaternary faults are from Macharé *et al.* [2003], Veloza *et al.* [2011], and <http://neotec-opendata.com>. The intercordillera complex fault system delimits the Western Cordillera from the Eastern Cordillera. The focal mechanism for $M > 5$ earthquakes were taken from the gcmt catalogue (black beach balls) and from local seismological studies [Suarez *et al.*, 1983; Devlin *et al.*, 2012; Ekström *et al.*, 2012]. The rectangles (blue dashed lines) follow the slab geometry used in the modeling (Table 1). Normal trench sections (dotted lines) are shown in Figure S1.

2014] but clearly show a compressional component. The focal mechanisms seen in the Altiplano are shallow and predominantly show an extensional component, although this intermountain basin is limited and deformed by two important convergent thrust systems [Baby *et al.*, 1997; Armijo *et al.*, 2015]. Their proximity to the Andean peaks or volcanoes probably reflects a local shallow extension controlled by gravitational processes rather than tectonic.

2.3. Fractures and Ridges on the Nazca Plate

Along the Peruvian trench, the most prominent subducting geomorphological structures that are clearly identified on the oceanic Nazca Plate are from north to south: the Alvarado Ridge (AR), Grijalva Ridge (GR), Sarmiento Ridge (SR), Virú Fracture Zone (VFZ), Mendaña Fracture Zone (MFZ), Nazca Ridge (NR), and Nazca Fracture Zone (NFZ) (Figure 1). These structures are thought to play a major role in the segmentation of the subduction zone earthquake-cycle processes [Sparks *et al.*, 2010; Wang and Bilek, 2014]. The locations of the MFZ and the NR, which delimit the central Peru segment, correlate with the rupture limits of the great 1746 ($M_w=8.8\text{--}9.0$) Lima-Callao earthquake. Because no known large or great earthquakes have ruptured across these structures, they could be considered to be strong and persistent barriers to the seismic rupture propagation [Perfettini *et al.*, 2010; Chlieh *et al.*, 2011; Nocquet *et al.*, 2014]. Smaller fracture zones like the NFZ can also stall the rupture propagation, as occurred during the 2001 ($M_w=8.4$) Arequipa earthquake [Robinson *et al.*, 2006] and probably also during the 1784 earthquake. However, the NFZ could also let the rupture propagate across, as occurred in the great 1604 and 1868 earthquakes, suggesting that it is a weak barrier. How the presence of these structures influences the seismic segmentation of the Peruvian megathrust is an important open question regarding the seismic hazard in that region.

3. GPS Data Sets and Processing

3.1. Data and Method

In addition to the data presented in Nocquet *et al.* [2014], we here use 51 new GPS measurements collected between 2008 and 2013 (Figure S2 and Table S2 in the supporting information). This new data set includes 28 continuous GPS (cGPS) stations from the Instituto Geográfico Nacional del Perú and 8 cGPS stations from the Low Latitude Ionospheric Sensor Network project (Instituto Geofísico del Perú (IGP)) installed in central and northern Peru [Valladares and Chau, 2012]. We also use 15 survey-mode GPS (sGPS) data sets from three profiles across the Andes Cordillera and the Subandean regions of northern Peru (at latitude 6°S) and central Peru (at latitudes 10°S and 12°S) from the French Institut de Recherche pour le Développement (IRD) and the Instituto Geofísico del Perú (IGP). In total, the final GPS data set is composed of 48 cGPS and 54 sGPS sites located from southern Ecuador (latitude 2.8°S) to southern Peru (latitude 18°S). The sGPS velocities are derived from at least three campaigns that were performed every 2 years starting from 2008. All of the cGPS velocities benefit from at least 2.5 years of measurement, the minimum period required to avoid bias from seasonal contributions to the velocity estimates [Blewitt and Lavalle, 2002]. Details about the data acquisition are provided in the supporting information.

Both survey-mode and continuous GPS data were simultaneously analyzed for the period of 2007.60–2013.75. The analysis was carried out using the GAMIT/GLOBK software (v10.50) [Herring *et al.*, 2010] in three steps. In the first step, we produced daily loosely constrained solutions, meaning that the relative station coordinates were well determined but not properly expressed in a well-defined reference frame. In the second step, we expressed the daily solutions in the International Terrestrial Reference Frame (ITRF) 2008 [Altamimi *et al.*, 2012] using a seven-parameter Helmert transformation estimated from the sites common to our solution and global sites from the International Global Navigation Satellite Systems Service (<http://igscb.jpl.nasa.gov>). For continuous stations, position outliers and offsets due to antenna changes were automatically identified and removed. Then, each time series was visually inspected to remove the remaining outliers using the Pyacs package [Tran, 2013] and Tsvview, a MATLAB toolbox [Herring and McClusky, 2009]. We excluded data between 2009.1 and 2009.7 near the peninsula of Bayovar in northern Peru because a transient slow slip event signal occurred at that period [Villegas-Lanza *et al.*, 2016]. The average repeatability values for the east, north, and vertical components of the daily station position were 1.5, 1.5, and 5.0 mm, respectively. A weighted linear regression was then used to fit the obtained time series to a model consisting of a linear trend, seasonal variations (for cGPS), and offsets. Finally, in the third step, after all of the outliers and offsets had been properly identified, the daily solutions were passed through a Kalman filter implemented in GLOBK in order to estimate a consistent set of coordinates and velocities with respect to the ITRF2008, together with the associated variance-covariance matrix. All of the velocity uncertainties account for the time-correlated noise in the GPS time series (more details are provided in the supporting information and Figure S12).

3.2. Definition of the Stable South American Reference Frame

In order to analyze the crustal deformation, the GPS velocities are expressed with respect to a stable South American (SSA) reference frame. We estimate a rigid rotation vector for the South American Plate using a subset of 20 sites that behave rigidly, following the criterions of *Nocquet et al.* [2001]. We find that a subset of 12 sites located on the South American Craton defines the optimal stable reference frame ($wrms = 0.40 \text{ mm/yr}$). The motion of the South America Plate relative to ITRF2008 is defined by an Euler pole located at 18.66°S , 132.72°W with an angular velocity of $0.118^\circ/\text{Myr}$ (Figure S3 and Table S3). These values are very similar to the solutions from *Altamimi et al.* [2012] and *Nocquet et al.* [2014]. Table S3 lists the GPS velocities along with their associated formal errors with respect to SSA.

4. Main Patterns of GPS Velocity Field

Our GPS velocity field samples the entire Peruvian and southern Ecuador margin. Figure 3 shows the GPS velocity field relative to SSA. Four main trends can be observed:

1. In northwestern Peru (north of latitude 9.5°S) and in southern Ecuador, the velocity field shows a fairly consistent southeastward motion of $\sim 5\text{--}6 \text{ mm/yr}$ with respect to SSA, in agreement with the results found by *Nocquet et al.* [2014]. In particular, no clear shortening in the plate convergence direction is observed, indicating a very small contribution from the interseismic elastic strain rate induced by mechanical coupling along the megathrust (Figure S6).
2. In northeastern Peru, the GPS velocities reveal a transition across the Marañon Valley that separates the Western and Eastern Andean Cordilleras (Figure 3). The GPS velocities in the Piura Peninsula indicate a southeastward motion of $\sim 5 \text{ mm/yr}$, and the velocities of the Eastern Cordillera and Subandean regions (near Tarapoto and Pucallpa) indicate an eastward motion of $1\text{--}3 \text{ mm/yr}$. The GPS direction of the sites located in the Eastern Cordillera and Subandean regions agrees with the direction of shortening accommodated across northwest-southeast reverse trending faults in the Subandean domain [*Macharé et al.*, 2003; *Veloza et al.*, 2011; *Eude et al.*, 2015] and with the observed reverse focal mechanisms [*Suarez et al.*, 1983; *Devlin et al.*, 2012] (Figure 3).
3. In central Peru, high velocities along the plate convergence direction are observed. These velocities decrease systematically inland as the distance from the trench increases. Maximum rates of up to 22 mm/yr are found in the San Lorenzo island located about 7 km offshore Lima. There are also significant lateral variations of velocities along the coast, with lower rates north and south of Lima, reflecting lateral variations in the interseismic coupling along the subduction interface.
4. In southern Peru, high velocities ($14\text{--}20 \text{ mm/yr}$) in the coastal area indicate significant coupling. Lateral variations are also seen, notably at the NR latitude, where lower velocities (8.5 mm/yr), about half of the magnitude of neighboring GPS sites, suggest a lower mechanical coupling on the subduction interface at this location. The obtained velocity field significantly differs from those collected before the 2001 Arequipa earthquake in the same area [*Norabuena et al.*, 1998; *Kendrick et al.*, 2001; *Chlieh et al.*, 2011]. We explain the reasons for this discrepancy in the discussion (section 6.2.4).

The velocity field therefore reflects the superimposed effects of both contributions coming from spatially heterogeneous coupling along the subduction interface and the long-term deformation of the overriding continent. With the new GPS measurements acquired in the Andes Cordillera and the Subandean regions, we find differences between the orientations of the GPS velocities located on the Western Cordillera and Eastern Cordillera. This first-order observation suggests that the previously defined Inca Sliver does not encompass the Subandean regions as initially thought. To avoid confusion with the previously defined Inca Sliver from *Nocquet et al.* [2014], we define the Peruvian Forearc Sliver (PS) as extending from the trench axis to the boundary between the Eastern and Western Cordilleras. From a direct inversion of a subset of 36 GPS measurements located on the PS and showing a coherent motion in the SSA reference frame, we find that a PS Euler pole relative to a stable South America (PS/SSA) located in the north of Colombia at 73.66°W and 4.26°N with an angular velocity of $0.215^\circ/\text{Myr}$ explains relatively well the motion observed in the GPS data (see Figure S4 and Table 2).

5. Heterogeneous Interseismic Coupling and Partitioning Model

In order to model the interseismic coupling along the megathrust interface and the rigid motion of the PS, we use a back slip approach [*Savage*, 1983] to model the GPS data in a fixed PS reference frame. We define a fault

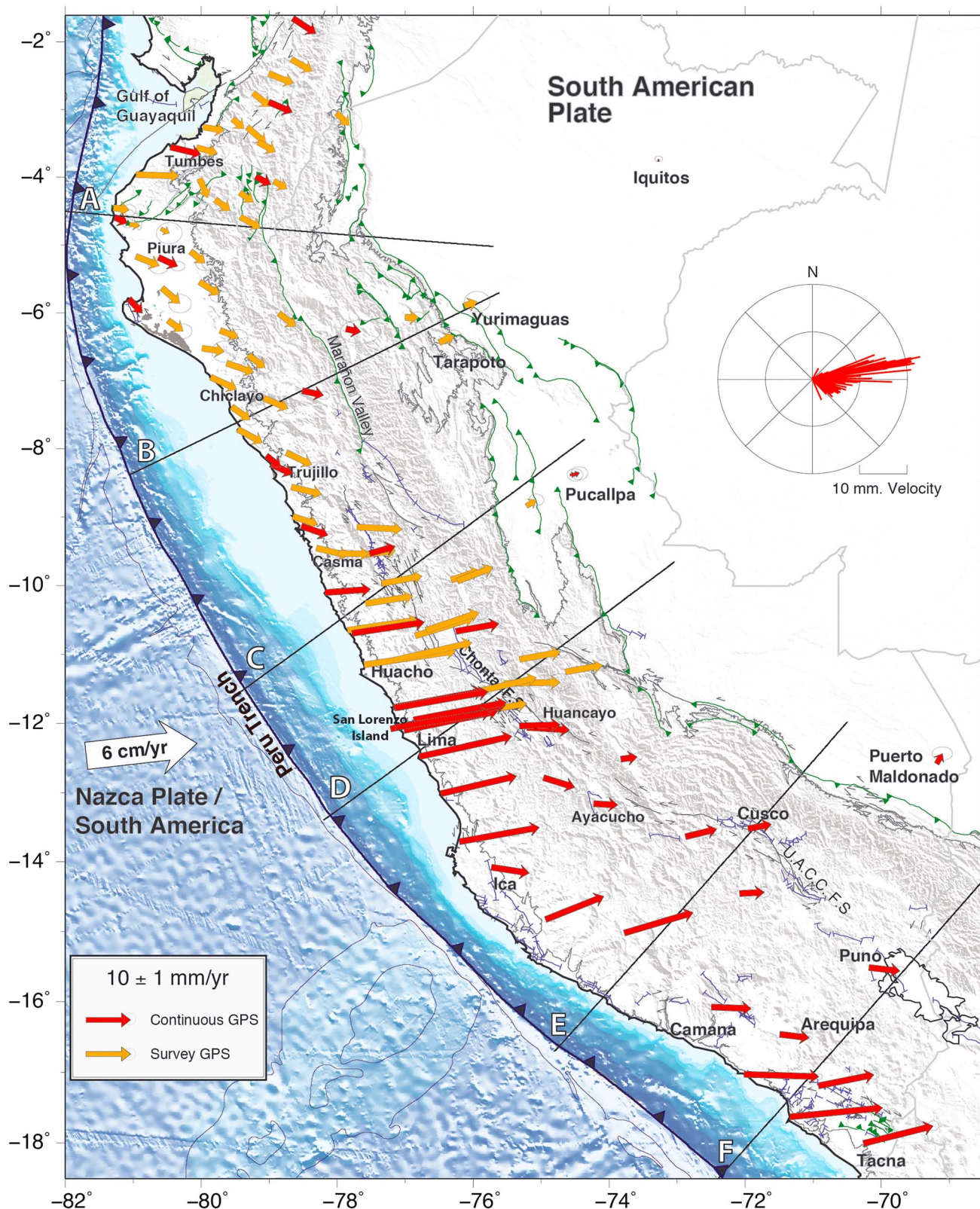


Figure 3. GPS velocity field expressed with respect to the SSA reference frame. The red and orange arrows correspond, respectively, to continuous (cGPS) and survey (sGPS) velocities. The GPS velocity field shows a complex pattern of deformation that considerably varies from northern to southern Peru (see the text for a description). The southeastward motion of sites in northern Peru shows an azimuth of 100° – 135° . The rose diagram is dominated by the eastward direction of the GPS vector, consistent with the plate convergence direction. Profiles A–F area reported in Figure S6.

Table 1. Fault Geometry of the Rectangular Dislocations Used in This Study to Describe the Megathrust Interface

Segment	Geographical Location	Southwestern Corner (Longitude, Latitude)	Length (km)	Strike (deg)	Dip (deg)
1	Southern Peru	71.2°W, 19.6°S	780	312	20
2	Central Peru	76.7°W, 14.9°S	620	324	15
3	North Peru	80.0°W, 10.4°S	460	334	12
4	Piura Peninsula	81.9°W, 6.5°S	460	5	12

geometry (section 5.1) composed of source points that roughly follow the slab interface. In the inversion procedure (section 5.2), we apply to each source point the average rake found from the regional focal mechanisms of the gCMT catalogue (see Figure S5) and a maximum back slip dislocation amplitude bounded by the relative Nazca/PS convergence rate. The first interseismic coupling inversion assumes no motion for the PS (section 5.3), and the GPS residuals are analyzed to constrain the location of the Peruvian Sliver Euler pole. Then, by varying the Euler pole velocity, we search for the best GPS fitting partitioning model. Finally, we explore a full range of interseismic coupling models (section 5.5) within the uncertainties of the GPS data and the resolution power of the GPS network.

5.1. Finite Fault Approach

The ground deformation at a GPS station produced by the slip on a finite fault can be determined by summing over the contributions of a regular grid of subfaults [i.e., Hartzell and Heaton, 1983; Hartzell *et al.*, 1996] as follows:

$$u = \sum_i \sum_j d_{ij} \left[\left(G_{ij}^s \cos(\lambda_{ij}) \right) + \left(G_{ij}^d \sin(\lambda_{ij}) \right) \right] \quad (1)$$

where u is the displacement at an arbitrary GPS station, i is the i^{th} subfault along-strike, and j is the j^{th} subfault along-dip. The terms G_{ij}^s and G_{ij}^d are the subfault Green functions for a unit slip in the strike direction and downdip direction, respectively. Each function is obtained by summing the responses of source points uniformly distributed over it. d_{ij} and λ_{ij} are the average dislocation slip and the rake angle, respectively. We adopt the above finite-fault description to define four rectangular dislocations (Figure 2) that follow the subduction interface geometry based on the Slab1.0 model [Hayes *et al.*, 2012] and modified by Nocquet *et al.* [2014]. The major difference is in the Lima area, where the Slab1.0 model predicts short-wavelength undulations that are not shown in the local seismicity catalogue and add unnecessary complexities to the model. Our defined slab geometry is embedded in a layered elastic half-space following the Crust2.0 model [Bassin *et al.*, 2000] (Table S6). The subfault parameters are listed in Table 1.

5.2. Inversion Procedure for Spatially Variable Interseismic Coupling

Using the finite-fault approach described above, the full representation of the fault response relies on two parameters: the dislocation amplitudes and rake angles. We can invert these parameters by fitting the static displacements to the observations. The general forward problem is written as follows:

$$\mathbf{d} = \mathbf{G} \cdot \mathbf{m} \quad (2)$$

where \mathbf{G} represents the Green's functions linking the observables to the model, \mathbf{d} is the data vector (here, the east and north components of the GPS velocities), and \mathbf{m} is the model vector (here, the back slip amplitude and rake direction). The inversion is performed using a simulated annealing algorithm called the heat-bath algorithm [Rothman, 1986]. Compared to other simulated annealing algorithms, it offers two advantages. First, it speeds up the calculation of the cost function by a factor of 100 or more because when the parameters of one subfault are perturbed, the response of the rest of the fault can be saved. Second, it is a recommended computational method for solving problems with a large number of free parameters [Sen and Stoffa, 1991; Tarantola, 2005]. Two types of regularization constraints can be chosen: one that minimizes the difference between the slip on adjacent subfaults and a second that minimizes the total moment (or moment deficit rate in the case of back slip) of the model [Hartzell *et al.*, 1996]. The corresponding cost function is written as follows:

$$\text{cost} = \text{wrms}^2 + \lambda_1 Dc^2 + \lambda_2 (Mo - M_d)^2 \quad (3)$$

where Dc represents the differences in the back slip rates of adjacent cells, Mo is an a priori moment deficit rate, and M_d is the final moment deficit rate for each source point. The coefficient λ_1 controls the smoothing

coefficient through an L1 + L2 norm [Sen and Stoffa, 1991]. The coefficient λ_2 modulates the weight assigned to minimize the final moment deficit rate [Ji et al., 2002]. In all of the models, we impose the back slip rate (V_{back}) to be lower or equal to the relative plate convergence rate (V_{pl}). The interseismic coupling (ISC) is defined as $0 \leq V_{\text{back}}/V_{\text{pl}} \leq 1$, resulting in pure creeping when ISC = 0 and full locking when ISC = 1. We impose the rake to remain within $\pm 10^\circ$ of the local average gCMT rake (see Figure S5). We fixed $\lambda_1 = 1$ based on the results of sensitivity tests reported in Figure S7. In the following sections (5.3 and 5.4), no constraint is imposed on the final moment deficit rate (i.e., $\lambda_2 = 0$). Finally, in section 5.5, we fix $\lambda_2 = 1$ and vary the final moment deficit rate.

5.3. Two-Plate Model and GPS Residuals Derived Euler Pole for the Peruvian Sliver

First, to test the robustness of the Peruvian Sliver kinematic found in a direct approach, we propose an independent analysis of the GPS residuals of a two-plate model as conducted in previous studies [Métois et al., 2012]. We performed an inversion of the GPS data in the SSA reference frame. Figure 4 shows the interseismic coupling map of a two-plate model, together with the GPS residual velocities. While the GPS residuals located in the Western Cordillera show a coherent pattern of southeastward motion, a systematic counterclockwise rotation is observed for sites located in the Eastern Cordillera and the Subandean domains. This transition seems to occur across the Marañón Fault System in the northern Peru and across the Chonta Fault System in central Peru (Figure 3). This can especially be seen between sites HNCO/HC01, TAPO/MRCD, and AP01/CUZC. Based on this first analysis, we can redefine the eastern boundary of the Peruvian Forearc Sliver, which encompasses the entire margin from northern to southern Peru and is limited by the oceanic trench axis and the boundary between the Western and Eastern Cordilleras. Using these new boundaries for the PS, we selected 36 GPS residual velocities located within the PS for which we inverted the Euler pole characteristics. We found that a PS/SSA Euler pole located at 67.23°W and 8.36°N with an angular velocity of $0.095^\circ/\text{Myr}$ explained the GPS residuals relatively well (see Table 2 and Figure S4).

The location of the PS/SSA Euler pole is consistent using the two approaches followed in this study: (1) a direct analysis of a subset of GPS data and (2) indirect analysis using the GPS residuals. Using both approaches, we find an Euler pole located near the boundary between northern Colombia and eastern Venezuela (see the inset of Figure S4). However, these methods lead to significantly different angular velocities, a bias linked intrinsically to the method used to determine the Euler pole characteristics. In order to account for the trade-off between the motion of the PS and the interseismic coupling along the subduction interface, we now consider a three-plate model (Nazca Plate, Peruvian Sliver, and South America) in which we fix the Euler pole location and vary the angular velocity to find the best GPS-fitting partitioning model.

5.4. Three-Plate Models

In order to properly account for the kinematics of the Peruvian Sliver, we take the PS/SSA Euler pole location (67.23°W and 8.36°N) found from the GPS residuals analysis above and vary exclusively its angular velocity from 0 to $0.22^\circ/\text{Myr}$ in steps of $0.05^\circ/\text{Myr}$. Note that for each inversion, it is important to adequately adjust the back slip rate (V_{back}) to equal the relative Nazca/PS convergence rate (Table S7). We find that the best GPS-fitting model works for a PS Euler pole having an angular velocity of $0.104 \pm 0.02^\circ/\text{Myr}$ (model 3-plate-C in Table 3), which predicts a southward motion of the Peruvian Sliver of 3.9 mm/yr in northern Peru and 5 mm/yr in southern Peru (Figure 5b). This implies that the Nazca/PS boundary absorbs about 55 mm/yr of the total convergence in central Peru. Figure 5a shows the resulting heterogeneous interseismic coupling map of the Peruvian subduction zone. This solution was found without any constraints on the final rate of moment deficit (i.e., $\lambda_2 = 0$) and tends to converge to a minimum moment deficit rate solution. In other words, in the low-resolution areas of the slab, no coupling would be applied if it is not needed by the data but could nonetheless exist (see resolution tests in Figure S8). To account for that uncertainty, we now fix $\lambda_2 = 1$ and explore a final family of acceptable solutions within the spatial resolution of the GPS network.

5.5. Variations in the Moment Rate Deficit

In previous sections, we imposed no constraint on the final moment deficit rate ($\lambda_2 = 0$). Here in order to account for the uncertainties in the low-resolution patches of the megathrust, we fix $\lambda_2 = 1$ and consider a series of models where the rate of moment deficit (M_d) is varied from $1.0 \times 10^{20} \text{ Nm/yr}$ ($M_w \sim 7.3$) to $7.0 \times 10^{20} \text{ Nm/yr}$ ($M_w \sim 7.9$) (Table S8). We find that models with a moment deficit rate between $2.4 \times 10^{20} \text{ Nm/yr}$ ($M_w \sim 7.6$) and $4.0 \times 10^{20} \text{ Nm/yr}$ ($M_w \sim 7.7$) fit the GPS data well (Figure S9). Figure 6 shows

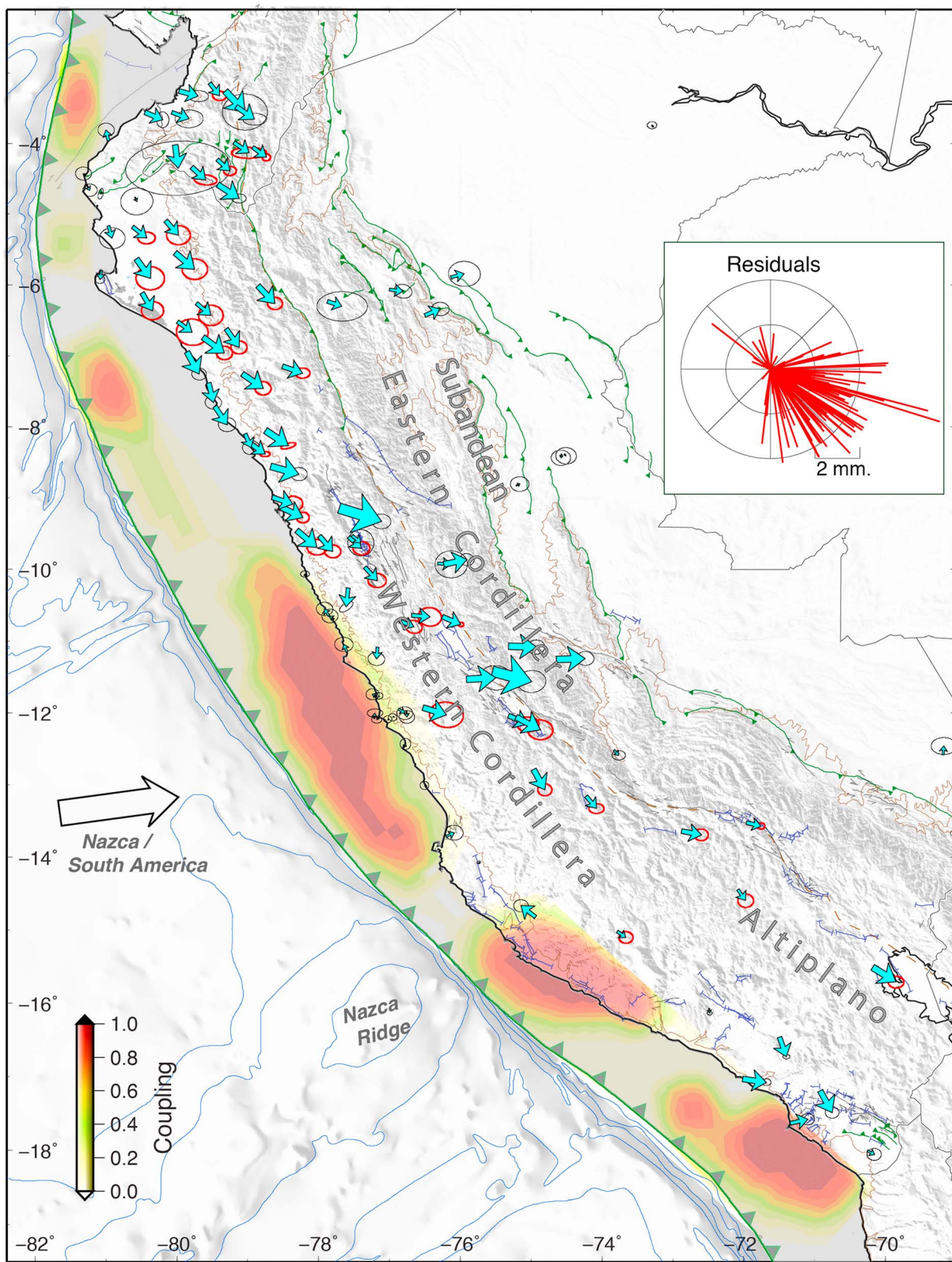


Figure 4. Two-plate model inversion of the GPS velocities in the SSA reference frame. The southeastward motion of the residuals (blue arrows) along the coastal regions and the Western Cordillera reflects the motion of the Peruvian Sliver from the Gulf of Guayaquil to the Arica Bend. The wind-rose diagram of residuals (inset) is another representation of the southeast direction of the GPS residual velocities. Table 2 contains the best fitting Euler pole for the Peruvian Sliver/SSA motion obtained from a subset of 34 GPS residuals (red ellipses).

Table 2. Characteristics of Rotation Poles for the Peruvian Sliver Relative to SSA^a

Pole Name	Method	No. of GPS Sites	Longitude (deg)	Latitude (deg)	Angular Velocity (°/Myr)	wrms	Reference
Inca/SSA	GPS data	28	63.76°W	22.47°N	0.092	0.83	Nocquet <i>et al.</i> [2014]
Peruvian/SSA	GPS data	36	73.66°W	4.26°N	0.215	0.66	This Study
Peruvian/SSA	Residuals	36	67.23°W	8.36°N	0.095	0.55	This Study
Peruvian/SSA	Residuals	36	67.23°W	8.36°N	0.104	0.40	This Study

^aColumns 2 and 3 show the method (direct GPS velocities/residuals) and number of GPS sites used to define the poles. Columns 4, 5, and 6 are the pole locations and angular velocities. On row 3, the GPS residuals are from the two-plate model and on row 4 from the three-plate model. The bold text shows our preferred model.

the family of acceptable interseismic coupling distributions, i.e., with a GPS misfit (wrms) lower than 2 mm/yr. The ISC appears to be heterogeneous at the scale of Peru, with weak and localized coupling found along the northern segment from latitude 10°S to 2°S near the Gulf of Guayaquil, a large area of high coupling in the central segment from latitude 10°S to 15°S and at least two ~100–200 km highly coupled asperities in the southern segment. When the moment deficit rate increases, the asperities widen and the coupling increases significantly near the trench where the GPS network provides no constraints. Spatial resolution checkerboard tests indicate that the along-strike spatial resolution is relatively high everywhere along the Peruvian margin. The along-dip resolution is also high in the Piura Peninsula, but decreases significantly further south, especially near the trench axis. The interpretation of shallow locking should be performed with more caution there (see Figure S8 and details in the supporting information). In this final test, we can see that the interseismic coupling distribution is quite robust along-strike but uncertainties about the coupling persist near the trench, where the data resolution is low to null, except offshore Lima, where sea bottom GPS data suggest shallow locking [Gagnon *et al.*, 2005]. Therefore, this test provides a family of models with a range of moment deficit rates that take into account the data uncertainties/resolution and the possibility that shallow coupling could exist, which has been a major issue for all subduction zones since the 2011 ($M_w = 9.0$) Tohoku earthquake.

6. Discussion

6.1. Tectonics of the Peruvian Margin

As with most subduction zones accommodating oblique convergence, the Nazca/SSA oblique convergence of 63 mm/yr is partitioned at the Peruvian margin. Figure 7 shows how the convergence is distributed among the relative motion between the Nazca Plate and the Peruvian Sliver (55 mm/yr), the rigid motion of the PS (4–5 mm/yr), and the Subandean crustal shortening relative to SSA (2–3 mm/yr). The velocity agreement between our proposed PS/SSA Euler pole and sites located in southern Peru as far as Puno (70.2°W, 15.5°S) support the fact that the Peruvian sliver might encompass, at least, the entire 2200 km long of the Peruvian Forearc Margin, from the Gulf of Guayaquil to the Arica Bend. The Peruvian Sliver motion trench-parallel component remains fairly constant all along Peru (~4 mm/yr; Figure 7). This trench-parallel motion agrees with the along-trench component of the Nazca/South America convergence vector, suggesting that the motion of the Peruvian Sliver is controlled by the obliquity of the plate convergence.

Although no internal deformation is detected within the Southern Cordillera in Ecuador, we find that in northern Peru there is an onset of strain and counterclockwise rotation at the boundary between the Western Cordillera and Eastern Cordillera across the Marañón Fault System. It has been suggested that the

Table 3. Characteristics of the Two-Plate and Three-Plate Models^a

Model Name	Peruvian Sliver Angular Velocity (°/Myr)	wrms (mm/yr)	Md Total 10^{20} Nm/yr
2-plate	0	3.79	3.82
3-plate-A	0.044	2.50	3.42
3-plate-B	0.084	1.77	3.00
3-plate-C	0.104	1.63	2.74
3-plate-D	0.124	1.75	2.51
3-plate-E	0.177	3.08	1.91
3-plate-F	0.199	3.92	1.65

^aColumn 2 shows the angular velocity of the Peruvian Sliver in °/Myr. Column 3 shows the misfit of the GPS data. Column 4 shows how the moment deficit rate Md of the model varies in 10^{20} Nm/yr. The text in bold shows our preferred model.

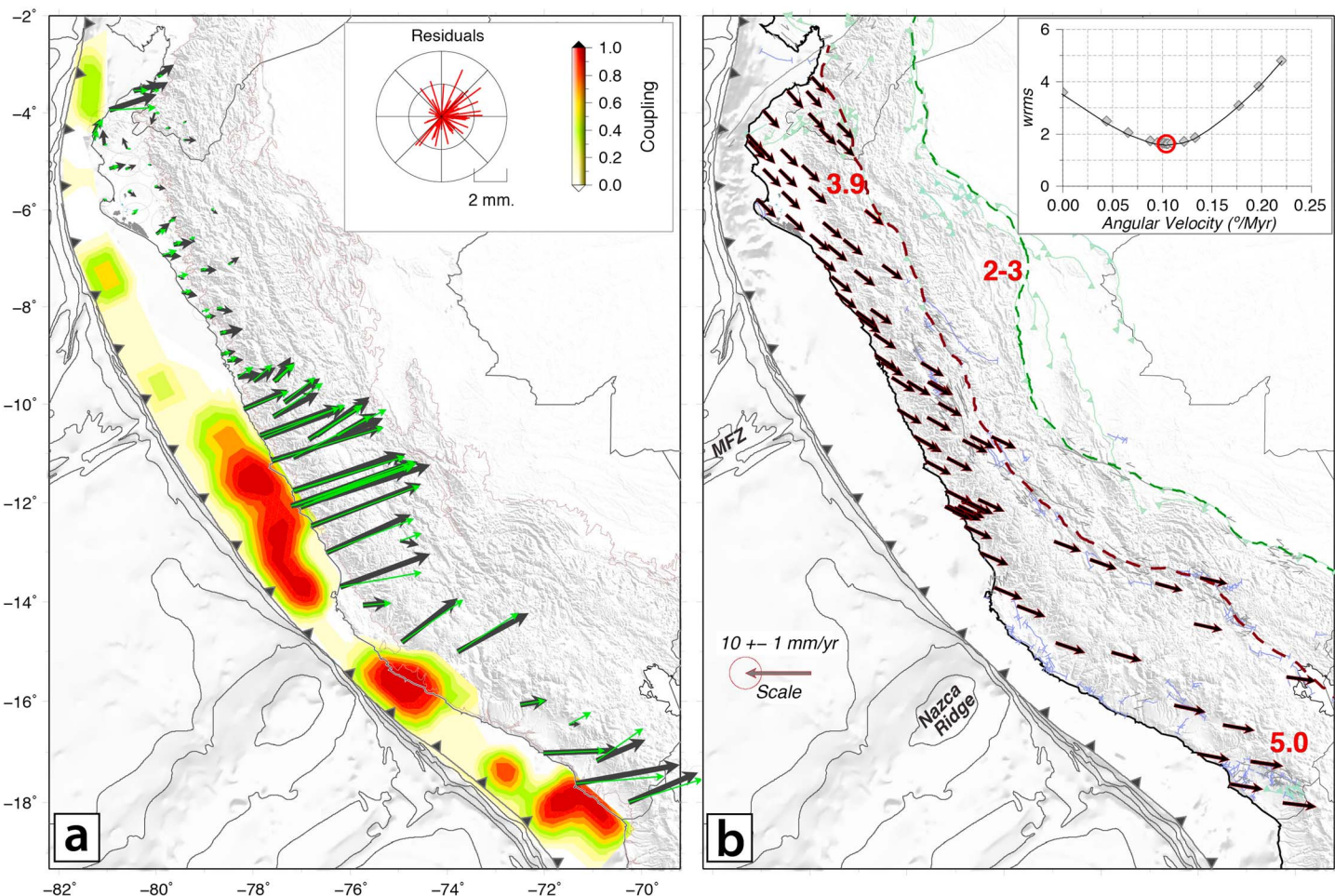


Figure 5. Best partitioning model considering rigid motion of Peruvian Sliver rotating southwestward relative to SSA and interseismic coupling model produced from inversion of GPS data in the Peruvian Sliver reference frame. (a) The observed and predicted interseismic GPS displacements are shown as black and green vectors, respectively. The wind-rose diagram of the GPS residuals (inset) shows residuals lower than 2 mm/yr in an azimuthally random distribution. (b) The rigid motion predicted from the PS/SSA Euler pole location (Table 2) and an angular velocity of 0.104°/Myr.

Marañon Fault is a reverse fault [Mégard, 1984; Carlotto *et al.*, 2009]; however, direct measurements of the relative motion at GPS sites located on both sides of the fault (sites CUYC and AM02) indicate a predominant left-lateral motion of 1.2–2.5 mm/yr. No clear fault-perpendicular motion can be reliably determined from the GPS data, but if it exists, it is smaller than 1 mm/yr. The GPS sites located east of the Marañon Fault move homogeneously eastward at a rate of 2–3 mm/yr. The present shortening rate is thus lower than 3 mm/yr, taken up by the fold and thrust belt located west of Yurimaguas. In central Peru, a short-scale gradient is seen in the velocity field between the Western Cordillera and Eastern Cordillera crossing the Chonta Fault System. Once corrected for our best interseismic subduction coupling model, the relative motion between the LRYA and TAPO sites located on each side of the Chonta Fault System is 2.5 ± 1.7 mm/yr of right-lateral motion and 1.0 ± 1.3 mm/yr of shortening. In southern Peru and northern Bolivia, GPS sites are scarce, which precludes the definition of the eastern limit of the Peruvian Sliver. However, geological data for southern Peru (INGEMMET maps; <http://geocatminapp.ingemmet.gob.pe/apps/geocatmin/> [Armijo *et al.*, 2015]) and northern Bolivia (YPFB unpublished maps) allow us to suggest that it corresponds to the western limit of the Altiplano, which has already been described as a strike-slip fault system [Rochat *et al.*, 1998].

In the Subandean zones, reverse faulting is evidenced by thrust focal mechanisms. This fault system limits the easternmost flank of the Eastern Cordillera and accommodates crustal shortening. The direction of shortening (NE) requires either a counterclockwise rotation of small Subandean blocks or shortening transfer zones (oblique or lateral ramps) in the eastern Andes with respect to the Peruvian Sliver. These accommodations are

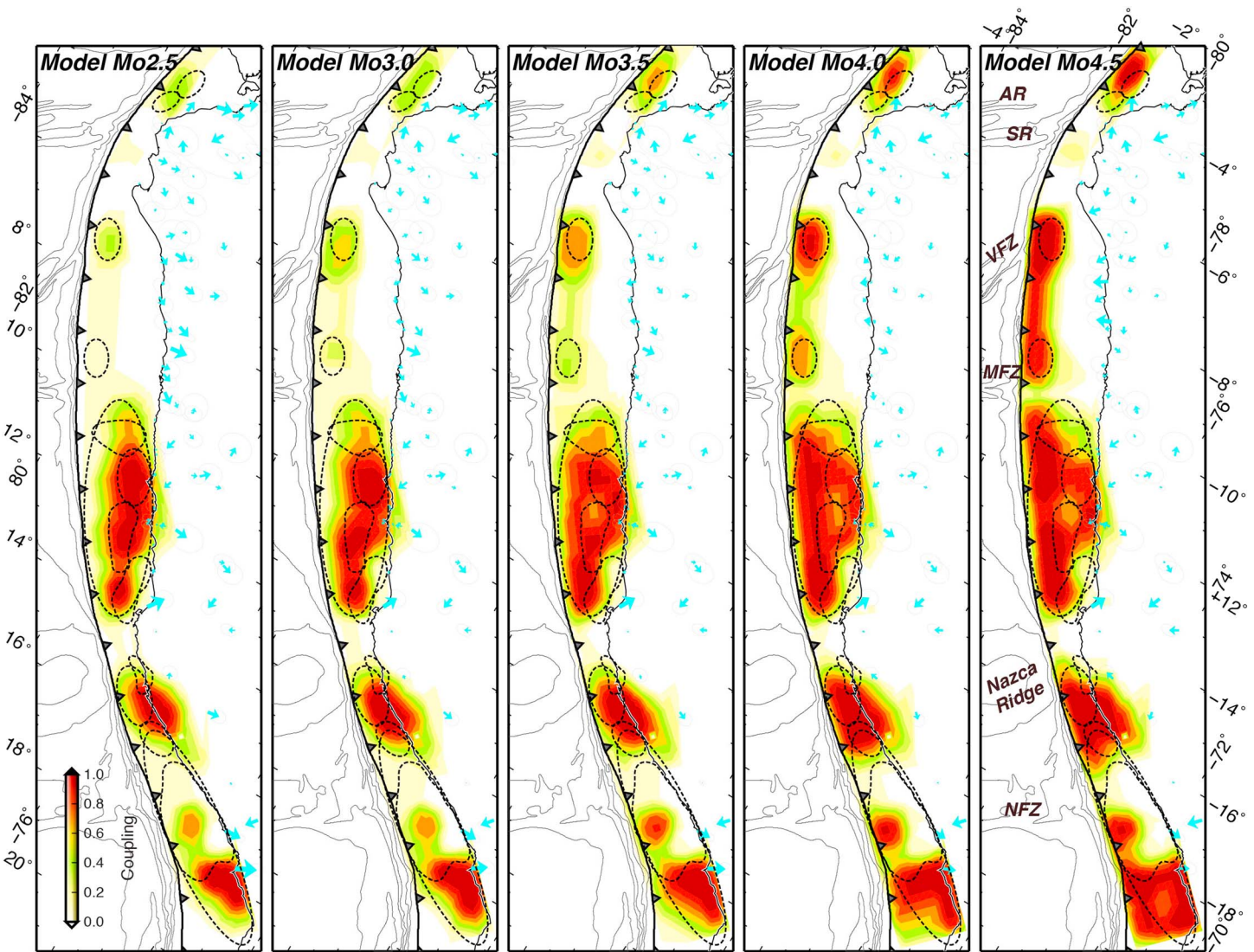


Figure 6. Best GPS fitting interseismic models with rate of moment deficit ranging from 2.4×10^{20} Nm/yr ($M_w \sim 7.6$) to 4.0×10^{20} Nm/yr ($M_w \sim 7.7$). The blue arrows show the GPS residuals. Increasing the rate of moment deficit extends the up-dip limit of the coupling near the trench, where the slip resolution is low and the uncertainties are the highest. Note that where the NR and fracture zones subduct, the ISC remains very low in all inversions.

particularly well represented in the central-southern segments transition with the counterclockwise rotation of the Cusco zone [Gilder et al., 2003] and the Tambo oblique ramp [Espurt et al., 2008]. Along the Eastern Andes, our Euler pole for the Peruvian Sliver would predict 4.5 mm/yr of motion in a 95°N direction with respect to SSA.

6.2. Interseismic Coupling Along the Peruvian Subduction Zone

In the following paragraphs, we compute the along-strike variations in the rate of moment deficit to better quantify the elastic strain accumulated on the megathrust interface.

6.2.1. Along-Strike Variations in the Rate of Moment Deficit

To quantify the along-strike variation in the interseismic coupling, we define the rate of moment deficit $dMo(t)/dt$ as follows:

$$\frac{dMo(t)}{dt} = \mu S \frac{d(v_o - v)(t)}{dt} \quad (4)$$

where $d(v_o - v)(t)/dt$ is the mean convergence rate (or back slip offset) across a surface S embedded in a medium with an average rigidity μ . Using this definition, we compute the along-strike variations in the rate of moment deficit for the best family of inversion models. The moment deficit is computed at each

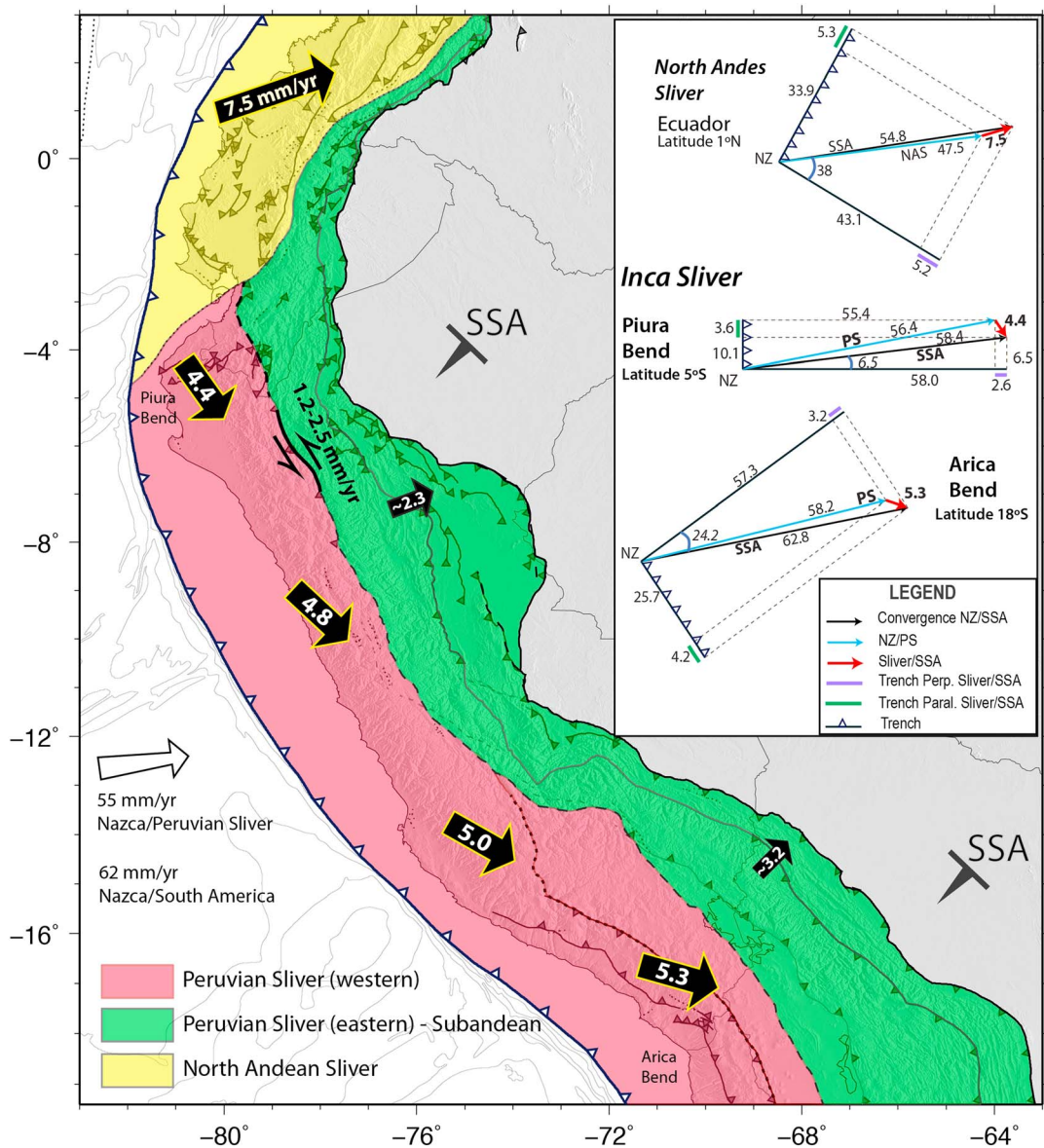


Figure 7. Schematic description of the principal continental slivers contributing to the deformation partitioning of the Peruvian margin: North Andean Sliver (NAS; yellow) Peruvian Sliver (PS; in red), and Eastern Cordillera–Subandean regions (in green), which are separated by the limit between Western Cordillera and Eastern Cordillera. All of the motions are in reference to SSA and are expressed in millimeters per year (mm/yr). The inset shows the kinematic triangles and obliquity partitioning vectors for Ecuador (latitude 1°N), the Guayaquil Bend (latitude 5°S), and the Arica Bend (latitude 18°S). The lines with triangle symbols indicate the local trench axis. The green and purple lines are, respectively, the along- and normal-trench components of Nazca/SSA convergence vector. The blue arrows indicate the Nazca/NAS and Nazca/PS convergence vectors, and the red arrows are the NAS/SSA and PS/SSA convergence vectors.

$20 \times 20 \text{ km}^2$ square node, taking into account its local back slip rate and rigidity. Then, we sum over the moment deficit of all the nodes within a 20 km wide strip normal to the trench. Figure 8 shows the rate of moment deficit variations along the 2200 km long Peruvian subduction zone. Although the final coupling models indicate differences, we can notice that at the scale of the entire Peruvian subduction zone, the integrated rate of moment deficit remains in a limited range (2.4 to 4.0×10^{20} Nm/yr) corresponding to an equivalent seismic moment magnitude (M_w of 7.6–7.7), which is yearly accumulated on the Peruvian megathrust interface (Figure 8 and Table S8). This integrated moment deficit rate hides fairly large local uncertainties, especially in the northern Peru, where extreme models can be significantly different due to the low shallow spatial resolution (see the uncertainties for northern Peru in Figure 8).

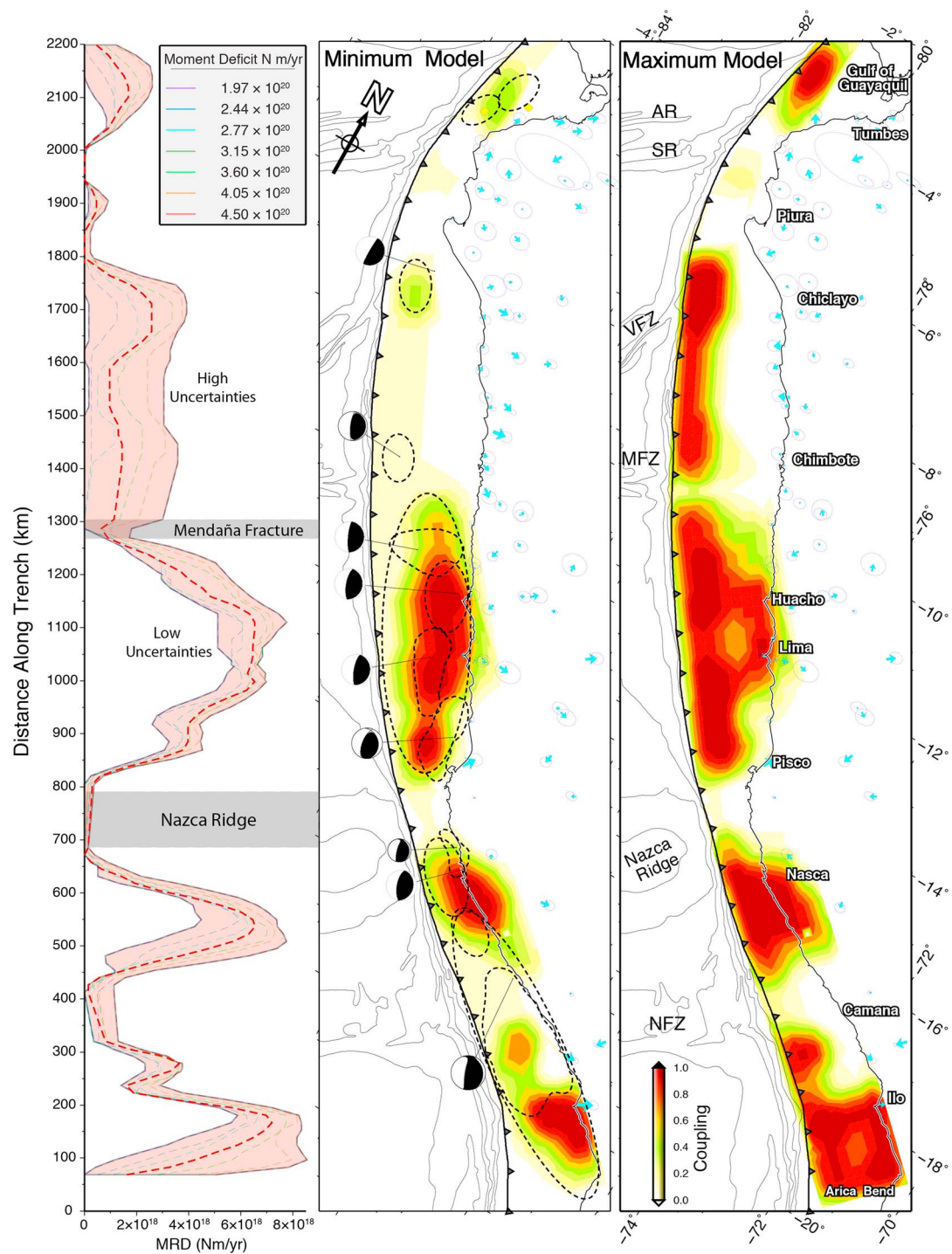


Figure 8. (left) Along-trench variations of moment deficit rate for (middle) minimum and (right) maximum interseismic coupling models. Even though the interseismic pattern might vary significantly between models, the locations of the peaks and valleys in the rate of moment deficit are very persistent characteristics that highlight the locations of the principal asperities (peaks) and creeping barriers (valleys). The dashed ellipse contours in the middle map show the approximate rupture area of large earthquakes, as described in Figure 1.

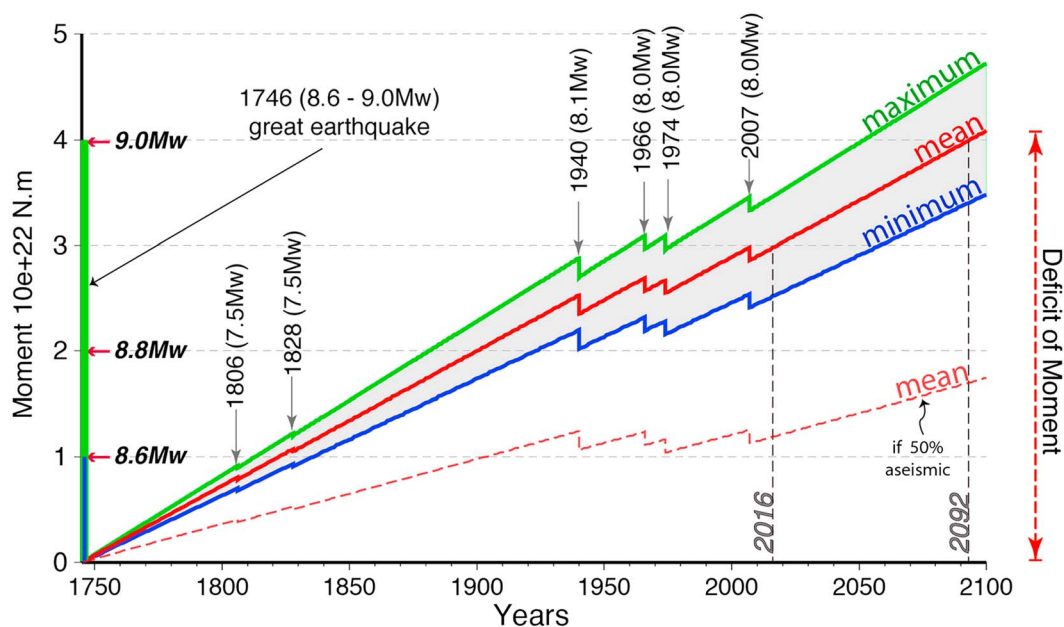


Figure 9. Cumulative moment deficit corrected from large earthquakes moment released since 1746, computed using the maximum, mean, and minimum interseismic models presented in Figure 6 and Table S8.

6.2.2. Shallow and Weak Coupling in Northern Peru

In northern Peru, the interseismic coupling appears to be confined within the shallowest 25 km of the slab interface, with local asperities having typical sizes of ~100 km along-strike and ~70 km along-dip (Figures 8 and 10). This pattern of coupling is in good agreement with the presence of shallow tsunami-earthquake asperities that, along with transient mixed-seismic-aseismic slip [Villegas-Lanza et al., 2016], might be the common mode of seismic behavior in the northern Peru segment. South of the Gulf of Guayaquil, a shallow asperity is found where the 1953 and 1959 tsunami-earthquakes occurred [Espinoza, 1992; Ioualalen et al., 2014]. Along the Piura peninsula, because the coastline is closer to the trench axis (~70–80 km), the spatial resolution is high and a very low interplate coupling is confirmed.

South of the Piura Peninsula, the coastal GPS data that extend from Chiclayo to Chimbote exclude the presence of interseismic coupling at depths greater than 30 km of the megathrust interface. Because the trench-to-coast distance between Chiclayo and northern Lima increases to nearly 200 km, the GPS network does not effectively resolve the pattern of coupling in the shallowest 30 km portion of the megathrust interface. Interseismic models suggest however the presence of two asperities that spatially correlate with the rupture areas of the 1960 and 1996 tsunami-earthquakes (Figures 8 and 10). Previous tsunami-earthquakes occurred in 1619 and 1759 in the rupture area of the 1996 ($M_w=7.6$) Chimbote earthquake [Ihmle et al., 1998; Bourgeois et al., 1999; Seiner Lizárraga, 2009; Spiske et al., 2013], suggesting an average return period of ~125 years.

One of the lessons that we learned from the great 2011 ($M_w=9.0$) Tohoku-Oki event is that the uncertainties in the shallow interseismic coupling should be taken into account. In the northern Peru segment (between Chiclayo and Chimbote), we find that the moment deficit rate could vary significantly (from 0.1 to 0.4×10^{20} Nm/yr, $\sim M_w=6.6\text{--}7.0$) because of the low resolution of the GPS data when attempting to accurately quantify the moment deficit rate there (Table S8 and Figure S10). Taking into account these uncertainties, the cumulative moment deficit will reach the equivalent of a $M_w\sim8.6\text{--}9.0$ event in about 1000 years, a period similar to the 1100 year recurrence time found for the Tohoku-Oki earthquake. Therefore, the seismic hazard in northern Peru should not be underestimated until seafloor GPS data are acquired and the shallow interseismic coupling is better evaluated.

6.2.3. High Coupling in the Central Peru Segment

Our models indicate a relatively high level of interseismic coupling in central Peru. This 550 km long segment is bounded on the north by the MFZ and on the south by the NR (Figures 8 and 10). Although the coupling

level close to the trench is not well constrained by the GPS data, the models indicate that a high interseismic coupling is required at depths up to 50 km of the megathrust interface. The annual moment deficit rate computed for the central Peru segment is $\sim 1.3 \times 10^{20}$ Nm/yr, corresponding to a moment magnitude earthquake of $M_w = 7.3$, that accumulates yearly on the central segment portion. The high coupling along the central Peru segment correlates well with the rupture area of the great 1746 megathquake (Figures 8 and 10). There is also a good spatial correlation between local interseismic asperities and the seismic sources of large $M_w \sim 8.0$ earthquakes that occurred in the central Peru segment between 1940 and 2007.

If we suppose that the interseismic strain is time invariant and purely elastic, we can compute the cumulative moment deficit corrected by the large seismic moments released since the great 1746 earthquake in central Peru (Figure 9). To do this, we integrate the moment deficit rate found from our best interseismic coupling model over the 1746 rupture area. We find that the cumulative moment deficit in 2016 is approximately the equivalent of an event with $M_w = 8.9$. At the actual moment deficit rate, we may reach the equivalent of an event with $M_w = 9.0$ event by the year 2092 (Figure 9). If we suppose that half of this moment deficit has been released through aseismic processes (postseismic relaxation, slow slip events, and seismic swarms), the moment deficit may still be the equivalent to $M_w = 8.7$ in 2016 and $M_w = 8.8$ in 2092. This indicates that the central Peru segment is quite mature and can host a great earthquake in the next decades, even though four large megathrust events have occurred since 1940.

6.2.4. High and Heterogeneous Coupling in the Southern Peru Segment

In southern Peru, interseismic coupling appears to be localized within two 100–150 km large asperities at latitudes of 16°S and 18°S (Figures 8 and 11). The northern asperity, located south of the NR, matches the rupture areas of the large 1913, 1942, and 1996 earthquakes. The southern asperity previously broke during the large 1833 earthquake and again during the great 1868 earthquakes. This area is able to host an event similar to the 2014 ($M_w = 8.2$) Pisagua earthquake [Ruiz et al., 2014; Álvarez et al., 2015]. In the rupture area of the 2001 Arequipa earthquake, we suspect that there is some ongoing postseismic deformation (see Arequipa cGPS time series in Figure S11), which gives the appearance of relatively low coupling there. Our coupling models indicate a relatively shallow and highly coupled patch that has a surface much smaller than the pre-2001 locked area [Norabuena et al., 1998; Bevis et al., 2001; Chlieh et al., 2011]. In addition, this highly coupled patch recovers the area of the high 2001 coseismic slip patch but does not recover the full 2001 rupture surface. All of these observations indicate that more than a decade after the 2001 ($M_w = 8.4$) event, only the area of high 2001 coseismic slip has been fully relocked, and long-term postseismic deformation may still affect that area, which has not reached its pre-2001 interseismic level.

6.3. Parameters Controlling the Seismogenic Behavior of the Megathrust

6.3.1. Along-Strike Seismic Segmentation

A key parameter suspected to control the lateral variations in the interplate coupling is the subduction of a topographic high or fracture on the seafloor (seamounts) [Watts et al., 2010; Wang and Bilek, 2014]. In regions where major geomorphologic features such as fracture zones and ridges intersect the trench axis, we notice a systematic local reduction of the interseismic coupling (Figures 8 and 10). These low-coupled regions correlate relatively well with the rupture extremities of large megathrust earthquakes, which supports the idea that the subduction of prominent geomorphologic structures play a key role in the segmentation and control of large subduction ruptures. The NR and MFZ bound the central Peru segment and are interpreted as robust seismic barriers because no historical large earthquakes ruptured through them. In southern Peru, the NFZ appears to act as a weak barrier that can sometimes stop or slow down a large seismic rupture, like it did during the 2001 Arequipa event [Robinson et al., 2006] and sometimes break with the neighboring asperities, as occurred during the great 1868 ($M_w = 8.8$) event. In northern Peru, the subduction zone is more segmented than in the central and southern segments, because of the entrance of five structures (the MFZ, the VFZ, SR, AR, and GFZ) separated by 100–250 km over a distance of 900 km along-trench (Figure 10). These structures may contribute to significantly lower the interplate coupling and play the role of barriers.

6.3.2. Along-Dip Thermal Control of the Coupling

Another fundamental category of models relates the coupling to the thermal steady state of the subduction interface, which itself depends on the age of the subducting plate, normal convergence rate, interface dip angle, and sediment thickness entering at the trench [Oleskevich et al., 1999]. To model the steady state thermal structure of the Peruvian megathrust interface we use the analytical expressions of Royden [1993], in which the heat transfer $\frac{\partial h}{\partial t}$ is solved in 2D using the following equation:

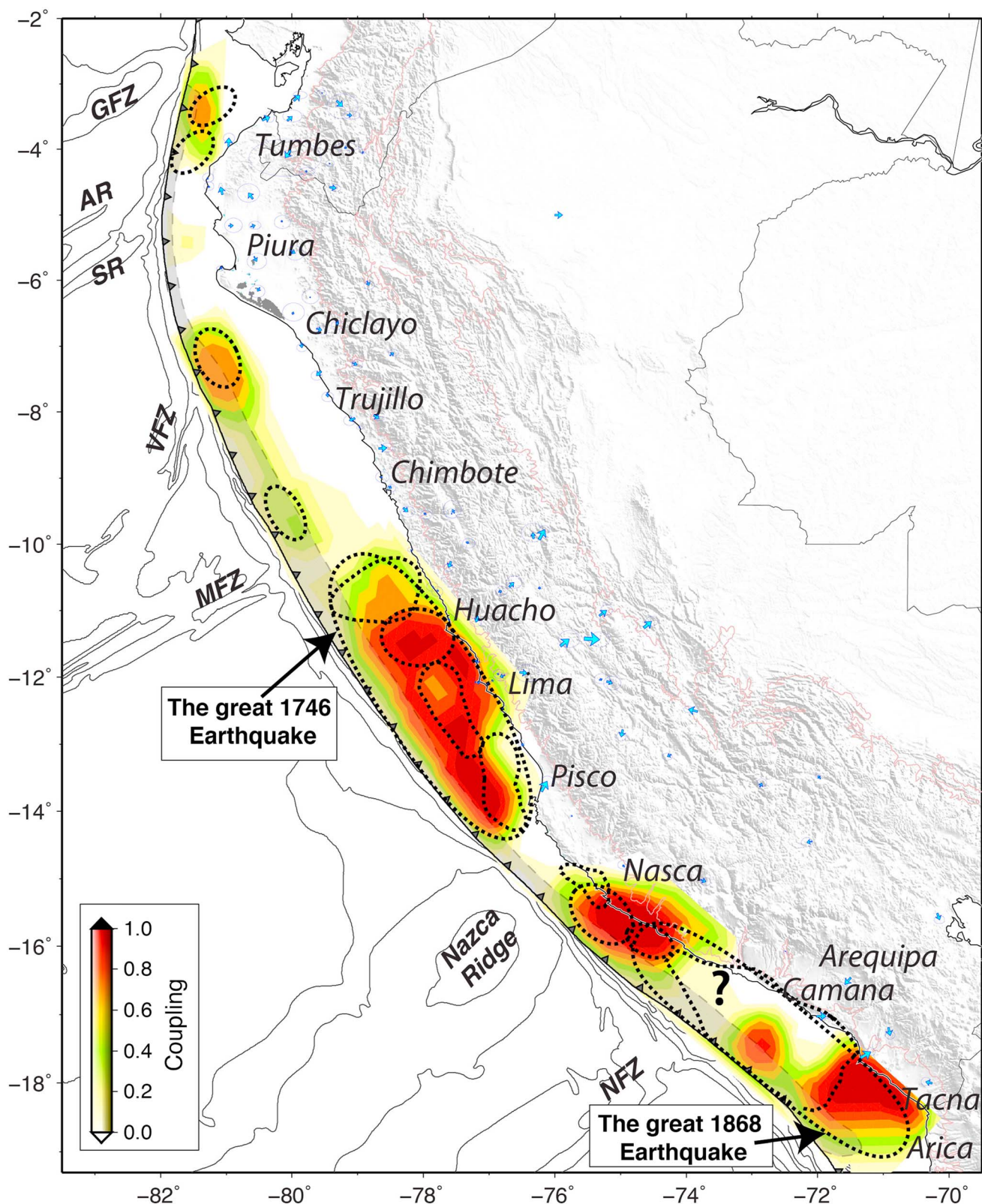


Figure 10. Average interseismic coupling model of Peru superimposed with recent and historical large earthquake ruptures. Where the NR and other fracture zones subduct, the ISC is very low. This supports the major role played by these geomorphological structures in the segmentation of the coupling and earthquakes. Note the high correlation between the past large ruptures and highly locked zones along the megathrust, except in the region of Arequipa, which is still affected by postseismic relaxation of the 2001 $M_w = 8.4$ earthquake. The gray shaded strip indicates the area where the model resolution is low.

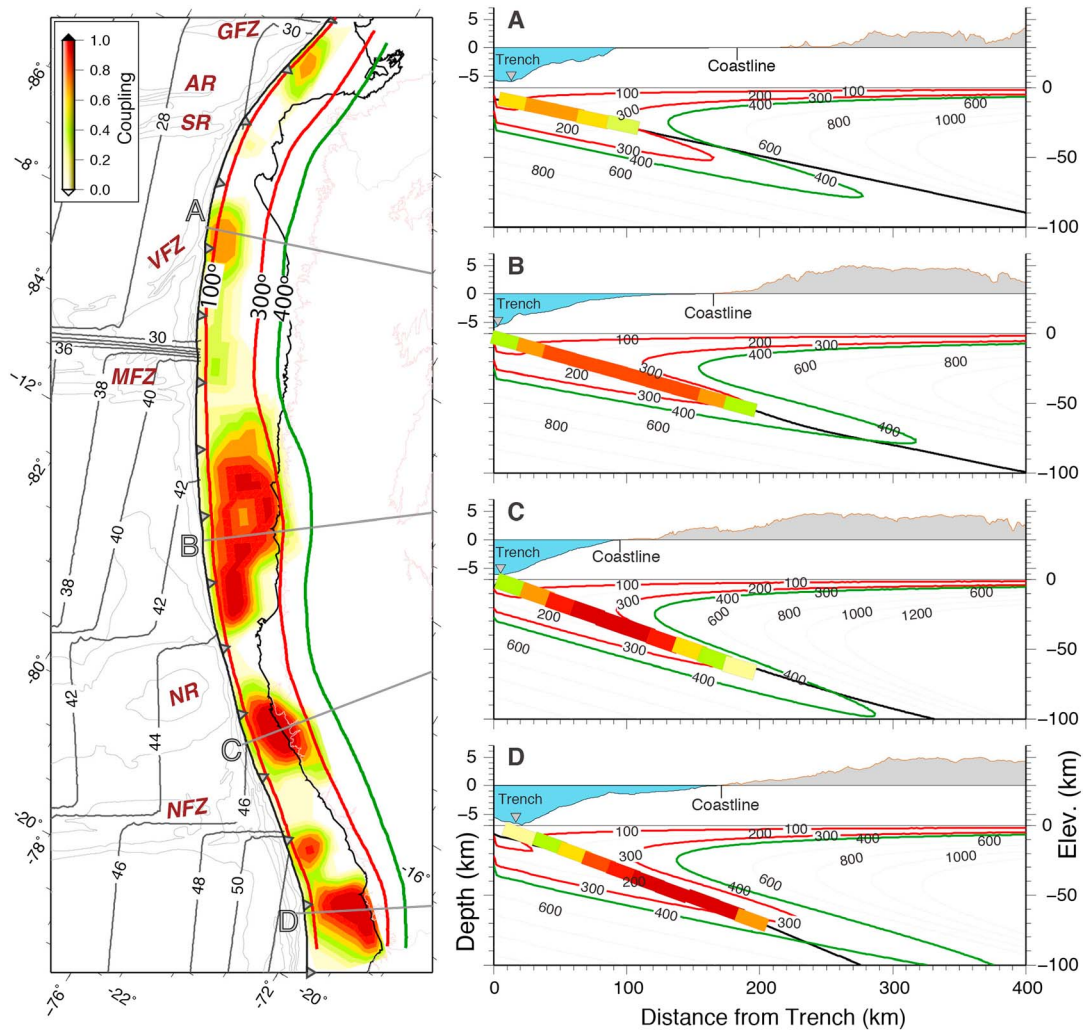


Figure 11. Steady state thermal structure of the Peruvian megathrust. (left) The age of the oceanic floor [Müller et al., 2008], which increases southward from 20 Ma north of the Gulf of Guayaquil to 55 Ma in southern Peru. Three major discontinuities appear in the ages of the oceanic seafloor at the Grijalva Fracture Zone (GFZ), where the ages are shifted from 20 Myr to 30 Myr, at the MFZ, with a jump from 29 Myr to 40 Myr, and at the NFZ, with a jump from 46 Myr to 51 Myr. The solid lines A, B, C, and D indicate the locations of the three sections shown on the right. (right) Normal-trench sections for A (Chiclayo), B (Lima), C (Nazca), and D (Moquegua), showing the bathymetry and topography from the GEBCO30s model. For each section, the steady state thermal model was computed using the slab geometry proposed by Hayes et al. [2012], along with the local normal convergence rate and age of the subducting Nazca Plate. In all the models, we apply a shear heating of 45 mW/m², except for profile A, where a shear heating of 20 mW/m² is applied.

$$\frac{\partial h}{\partial t} = k \nabla^2 T + v \frac{\partial t}{\partial z} + SH + R \quad (5)$$

where $k \nabla^2 T$ describes the term of conduction, $v \frac{\partial t}{\partial z}$ is the term of advection, SH is the shear heating, and R is the crustal radiogenic production. We assume a case where the radiogenic production is small (about 1.3 $\mu\text{W}/\text{m}^3$). The shear heating (fixed at 45 mW/m²) is calculated for a uniform shear stress of 40 MPa and a friction coefficient of 0.1. We fix the temperature at the base of the oceanic lithosphere at 1250°C. For the instantaneous heating or cooling of a semi-infinite half-space, the thickness H of the subducting plate is proportional to the thermal diffusion distance ($\kappa \times A$)^{0.5}:

$$H = 2.32 \times (\kappa \times A)^{0.5} \quad (6)$$

where κ is the thermal diffusivity (fixed at 1 mm²/s) and A is the age of the subducting plate [Turcotte and Schubert, 2002]. Following this relation, the thickness of the subducting plate increases from about 70 km in

northern Peru, where the age of the subducting oceanic plate is about 30 Ma, to 80 km in central Peru and about 90 km in southern Peru, where the oceanic seafloor age reaches about 45 Ma (Table S9). As a consequence of the change in the strike of the trench axis, the normal convergence rate decreases southward from about 58 mm/yr at the latitude of Chiclayo to 55 mm/yr at the latitude of Lima and 46 mm/yr at the latitude of Arequipa.

In the map view, the 100–300°C isotherms effectively bracket the locations of highly locked fault patches in central and southern Peru (Figure 11) but not in northern Peru, where the 300°C isotherm crosses the slab interface at about 20 km deeper than the downdip limit of the locked zone. We find that a reduction in the shear heating to 20 mW/m² or lower effectively reconciles the location of the 300°C isotherm with the downdip limit of the shallow locked zone found in northern of Peru (Figure 11, profile A). These simple thermal models support the conclusion that the thermal steady state may play a major role in controlling the along-dip interseismic coupling.

7. Conclusions

This study presented a detailed description of the deformation partitioning at the Peruvian margin. We define a Peruvian Sliver that extends N-S from the Gulf of Guayaquil to the Altiplano of Peru and E-W from the trench axis to the boundary between the Western Cordillera and the Eastern Cordillera. The Euler pole of the Peruvian Sliver relative to SSA is located at the boundary between northern Colombia and eastern Venezuela and predicts a rigid southeastward translation of the Peruvian Sliver at a rate of about 4–5 mm/yr with respect to SSA. The present-day Subandean shortening rates increase southward from 2 to 4 mm/yr.

With that new tectonic scheme, the relative motion between the Nazca Plate and the Peruvian Sliver is 55 mm/yr and is accommodated along the subduction megathrust interface. The resulting interseismic coupling of the Nazca megathrust interface appears to be highly heterogeneous, with low interseismic coupling, where geomorphologic structures on the Nazca Plate such as ridges and fracture zones enter in subduction. These structures appear to play a major role in the along-strike seismic segmentation of the Peruvian margin. The interseismic coupling map of Peru indicates that except for the extreme northern segment that extends up to the Piura Peninsula, all the other segments can host large to great earthquakes.

The northern Peruvian subduction segment extending from the Gulf of Guayaquil to the latitude of the Mendaña Fracture Zone is characterized by shallow and weak to moderate coupling. These asperities have a good spatial correlation with the location of shallow ruptures ($M_w \sim 7.5$) tsunami-earthquakes that occurred in 1953, 1960, and 1996. In contrast, the central Peru segment is highly coupled along an area that correlates well with the rupture area of the great 1746 ($M_w \sim 8.8$ –9.0) Lima-Callao earthquake. By assuming that the actual moment deficit rate integrated over the central Peru segment is time invariant, we found that today this segment could now host a great ($M_w \geq 8.5$) megathrust earthquake. In the southern Peru segment, in addition to the scarce density of coastal GPS sites and ongoing postseismic relaxation in the Arequipa region, our model shows two highly coupled asperities ~100–150 km long, one south of the Nazca Ridge at the latitude ~16°S and one between Tacna and Arica at the latitude ~18°S. The asperity at 16°S correlates well with the ruptures of the 1913 ($M_w \sim 8.2$), 1942 ($M_w \sim 8.2$), and 1996 ($M_w \sim 7.7$) subduction earthquakes. The Tacna-Arica asperity ruptured alone last time in 1833 and again during the great 1868 event but not during the 2001 Arequipa event. We believe that the Tacna-Arica asperity could host an event similar to the 2014 $M_w = 8.2$ Pisagua earthquake.

A caveat of this study is that the interseismic strain of the fore arc was assumed to be entirely elastic, neglecting any viscous mantle flow that could offer an alternate explanation for the sliver motion and reduce the interseismic coupling on the megathrust [Li et al., 2015]. We also neglected time variations in the rate of coupling during the interseismic period, which may affect the cumulative moment deficit and the recurrence time of great events.

References

- Abe, K. (1972), Mechanisms and tectonic implications of the 1966 and 1970 Peru earthquakes, *Phys. Earth Planet. Inter.*, 5, 367–379.
Altamimi, Z., L. Métivier, and X. Collilieux (2012), ITRF2008 plate motion model, *J. Geophys. Res.*, 117, B07402, doi:10.1029/2011JB008930.
Álvarez, O., S. Nacif, S. Spagnotto, A. Folguera, M. Giménez, M. Chlieh, and C. Braatenberg (2015), Gradients from GOCE reveal gravity changes before Pisagua $M_w = 8.2$ and Iquique $M_w = 7.7$ large megathrust earthquakes, *J. South Am. Earth Sci.*, 64, 273–287, doi:10.1016/j.jsames.2015.09.014.

Acknowledgments

This work has been financially supported by the Agence Nationale de la Recherche (ANR; contract number ANR-07-BLAN-0143-01) and has been continuously supported by the Institut de Recherche pour le Développement (IRD) and the Instituto Geofísico del Perú (IGP). We thank all the people of the Instituto Geográfico Nacional, Lima, Peru, and Instituto Geográfico Militar, Quito, Ecuador, for their work in maintaining permanent GPS networks. We also thank all the colleagues from IGP and IRD that have been involved in this project. This work has been possible through the support provided by the IRD-DSF and the IGP to J.C.V.L. We acknowledge additional support from the CNRS-INSU and RESIF-CORE for the use of the GPS-national pool. This work has been carried out in the frame of the Joint International Laboratory “Seismes et Volcans dans les Andes du Nord.” The data used in this study are available in the supporting information. We used the GMT software [Wessel and Smith, 1998] to prepare most of the figures. Finally, we thank L. Wallace, J. Loveless, and an anonymous reviewer for their comments and suggestions, which helped to improve this paper.

- Armijo, R., R. Lacassin, A. Coudurier-Carreleur, and D. Carrizo (2015), Coupled tectonic evolution of Andean orogeny and global climate, *Earth Sci. Rev.*, 143, 1–35, doi:10.1016/j.earscirev.2015.01.005.
- Arriagada, C., P. Roperch, C. Mpodozis, and P. R. Cobbold (2008), Paleogene building of the Bolivian Orocline: Tectonic restoration of the central Andes in 2-D map view, *Tectonics*, 27, TC6014, doi:10.1029/2008TC002269.
- Baby, P., P. Rochat, G. H. Mascle, and G. Herail (1997), Neogene shortening contribution to crustal thickening in the back arc of the central Andes, *Geology*, 25(10), 883–886.
- Bassin, C., G. Laske, and G. Masters (2000), The current limits of resolution for surface wave tomography in North America, *Eos Trans. AGU*, 81, F897.
- Beck, S. L., and L. J. Ruff (1989), Great earthquakes and subduction along the Peru trench, *Phys. Earth Planet. Inter.*, 57(3-4), 199–224, doi:10.1016/0031-9201(89)90112-X.
- Beck, S., S. Barrientos, E. Kausel, and M. Reyes (1998), Source characteristics of historic earthquakes along the central Chile subduction zone, *J. South Am. Earth Sci.*, 11(2), 115–1129, doi:10.1016/S0895-9811(98)00005-4.
- Bevis, M., E. Kendrick, B. Brooks, R. Allmendinger, B. Isacks, and R. Smalley Jr. (2001), On the strength of interplate coupling and the rate of back arc convergence in the central Andes: An analysis of the interseismic velocity field, *Geochem. Geophys. Geosyst.*, 2, 1067, doi:10.1029/2001GC000198.
- Bilek, S. L. (2010), Invited review paper: Seismicity along the South American subduction zone: Review of large earthquakes, tsunamis, and subduction zone complexity, *Tectonophysics*, 495(2), 2–14, doi:10.1016/j.tecto.2009.02.037.
- Bird, P. (2003), An updated digital model of plate boundaries, *Geochem. Geophys. Geosyst.*, 4(3), 1027, doi:10.1029/2001GC000252.
- Blewitt, G., and D. Lavalle (2002), Effect of annual signals on geodetic velocity, *J. Geophys. Res.*, 107(B7), 2145, doi:10.1029/2001JB000570.
- Bourgeois, J., C. Petroff, H. Yeh, V. Titov, C. E. Synolakis, B. Benson, J. Kuroiwa, J. Lander, and E. O. Norabuena (1999), Geologic setting, field survey and modeling of the Chimbote, northern Peru, tsunami of 21 February 1996, *Pure Appl. Geophys.*, 154, 513–540.
- Brooks, B. A., et al. (2011), Orogenic-wedge deformation and potential for great earthquakes in the central Andean backarc, *Nat. Geosci.*, 4(5), 1–4, doi:10.1038/ngeo1143.
- Carlotto, V., J. Quispe, H. Acosta, R. Rodriguez, D. Romero, C. Cerpa, M. Mamani, T. Velarde, and S. Lu y E Cueva (2009), Dominios geotectónicos y metalogénesis del Perú, *Bol. la Soc. Geolofgica del Peru*, 103, 1–89.
- Cembrano, J., F. Hervé, and A. Lavenu (1996), The Liquiñe Ofqui fault zone: A long-lived intra-arc fault system in southern Chile, *Tectonophysics*, 259(1-3), 55–66, doi:10.1016/0040-1951(95)00066-6.
- Chlieh, M., H. Perfettini, H. Tavera, J.-P. Avouac, D. Remy, J.-M. Nocquet, F. Rolandone, F. Bondoux, G. Gabaldá, and S. Bonvalot (2011), Interseismic coupling and seismic potential along the central Andes subduction zone, *J. Geophys. Res.*, 116, B12405, doi:10.1029/2010JB008166.
- Dalmayrac, B. (1978), *Geologie des Andes Péruviennes*, O.R.S.T.O.M, Paris.
- Delouis, B., J.-M. Nocquet, and M. Vallée (2010), Slip distribution of the February 27, 2010 $M_w = 8.8$ Maule earthquake, central Chile, from static and high-rate GPS, InSAR, and broadband teleseismic data, *Geophys. Res. Lett.*, 37, L17305, doi:10.1029/2010GL043899.
- Devlin, S., B. L. Isacks, M. E. Pritchard, W. D. Barnhart, and R. B. Lohman (2012), Depths and focal mechanisms of crustal earthquakes in the central Andes determined from teleseismic waveform analysis and InSAR, *Tectonics*, 31, TC2002, doi:10.1029/2011TC002914.
- Dewey, J. F., and S. H. Lamb (1992), Active tectonics of the Andes, *Tectonophysics*, 205, 79–95, doi:10.1016/0040-1951(92)90419-7.
- Diamant, M., H. Harjono, K. Karta, D. Depius, D. Dahrin, M. Zen, M. Gérard, O. Lassal, A. Martin, and A. Malod (1992), Mentawai fault zone off Sumatra: A new key to the geodynamics of western Indonesia, *Geology*, 20(March), 259–262.
- Dorbath, L., A. Cisternas, and C. Dorbath (1990), Assessment of the size of large and great historical earthquakes in Peru, *Bull. Seismol. Soc. Am.*, 80(3), 551–576.
- Ego, F., M. Sévrier, A. Lavenu, H. Yepes, and A. Egues (1996), Quaternary state of stress in the northern Andes and the restraining bend model for the Ecuadorian Andes, *Tectonophysics*, 259(1-3), 101–116, doi:10.1016/0040-1951(95)00075-5.
- Ekström, G., M. Nettles, and A. M. Dziewonski (2012), The global CMT project 2004–2010: Centroid-moment tensors for 13,017 earthquakes, *Phys. Earth Planet. Inter.*, 201, 1–9.
- Espinosa, J. (1992), Terremotos tsunamigenicos en el Ecuador, *Acta Ocean. del Pacific.*, 7(1), 1–8.
- Esput, N., F. Funiciello, J. Martinod, B. Guillaume, V. Regard, C. Faccenna, and S. Brusset (2008), Flat subduction dynamics and deformation of the South American plate: Insights from analog modeling, *Tectonics*, 27, TC3011, doi:10.1029/2007TC002175.
- Eude, A., M. Roddaz, S. Brichau, S. Brusset, Y. Calderon, P. Baby, and J.-C. Soula (2015), Controls on timing of exhumation and deformation in the northern Peruvian eastern Andean wedge as inferred from low-temperature thermochronology and balanced cross section, *Tectonics*, 34, 715–730, doi:10.1002/2014TC003641.
- Gagnon, K., C. D. Chadwell, and E. O. Norabuena (2005), Measuring the onset of locking in the Peru-Chile trench with GPS and acoustic measurements, *Nature*, 434(7030), 205–208, doi:10.1038/nature03412.
- Gilder, S., S. Rousse, D. Farber, B. McNulty, T. Sempere, V. Torres, and O. Palacios (2003), Post-Middle Oligocene origin of paleomagnetic rotations in Upper Permian to Lower Jurassic rocks from northern and southern Peru, *Earth Planet. Sci. Lett.*, 210(1-2), 233–248, doi:10.1016/S0012-821X(03)00102-X.
- Giovanni, M. K., S. L. Beck, and L. Wagner (2002), The June 23, 2001 Peru earthquake and the southern Peru subduction zone, *Geophys. Res. Lett.*, 29(21), 2018, doi:10.1029/2002GL015774.
- Hartzell, B. Y. S. H., and T. H. Heaton (1983), Inversion of strong motion and teleseismic waveform data for the fault rupture history of the 1979 Imperial Valley, California, earthquake, *Bull. Seismol. Soc. Am.*, 73(6), 1553–1583.
- Hartzell, S., A. Leeds, A. D. Frankel, and J. Michael (1996), Site response for urban Los Angeles using aftershocks of the Northridge earthquake, *Bull. Seismol. Soc. Am.*, 86(1B), S168–S192.
- Hayes, G. P., D. J. Wald, and R. L. Johnson (2012), Slab1.0: A three-dimensional model of global subduction zone geometries, *J. Geophys. Res.*, 117, B01302, doi:10.1029/2011JB008524.
- Herring, T. A., R. W. King, S. C. Mcclusky, and P. Sciences (2010), Documentation of the MIT. GPS analysis software: GAMIT release 10.40. *Mass. Inst. of Technol., Cambridge* (2010).
- Herring, T., and S. Mcclusky (2009), GAMIT/GLOBK MATLAB tools, *GPS Solut.*, 7(3), 194–199, doi:10.1007/s10291-003-0068-0.
- Ihmle, P. F., J.-M. Gomez, P. Heinrich, and S. Guibourg (1998), The 1996 Peru tsunamigenic earthquake: Broadband source process, *Geophys. Res. Lett.*, 25, 2691–2694, doi:10.1029/98GL01987.
- Ioulalalen, M., et al. (2014), Tsunami mapping in the Gulf of Guayaquil, Ecuador, due to local seismicity, *Mar. Geophys. Res.*, 35(4), 361–378, doi:10.1007/s11001-014-9225-9.
- Ji, C., D. J. Wald, and D. V. Helmberger (2002), Source description of the 1999 Hector Mine, California, earthquake, Part I: Wavelet domain inversion theory and resolution analysis, *Bull. Seismol. Soc. Am.*, 92(4), 1192–1207.

- Kelleher, J. A. (1972), Rupture zones of large South American earthquakes and some predictions, *J. Geophys. Res.*, **77**, 2087–2103, doi:10.1029/JB077i011p02087.
- Kendrick, E., M. Bevis, R. Smalley Jr., and B. Brooks (2001), An integrated crustal velocity field for the central Andes, *Geochem. Geophys. Geosyst.*, **2**, 11, doi:10.1029/2001GC000191.
- Kendrick, E., M. Bevis, R. S. Jr., B. Brooks, R. Barriga, E. Lauria, and L. P. S. Fortes (2003), The Nazca-South America Euler vector and its rate of change, *J. South Am. Earth Sci.*, **16**, 125–131.
- Li, S., M. Moreno, J. Bedford, M. Rosenau, and O. Oncken (2015), Revisiting viscoelastic effects on interseismic deformation and locking degree: A case study of the Peru-North Chile subduction zone, *J. Geophys. Res. Solid Earth*, **120**, 4522–4538, doi:10.1002/2015JB011903.
- Lockridge, P. A. (1985), Tsunamis in Peru-Chile, Report SE-39, Boulder, WDC-A for Solid Earth Geophysics, 97p.
- Macharé, J., C. H. Fenton, M. N. Machette, C. Costa, and R. L. Dart (2003), Database and map of quaternary faults and folds in Peru and its offshore region. *USGS Open-File Report 03-451*.
- Mccaffrey, R. (2002), Crustal block rotations and plate coupling, in *Plate Boundary Zones*, edited by S. Stein and J. Freymueller, pp. 101–122, AGU, Washington, D. C.
- Mégard, F. (1984), The Andean orogenic period and its major structures in central and northern Peru, *J. Geol. Soc. London.*, **141**, 893–900, doi:10.1144/gsjgs.141.5.0893.
- Métois, M., A. Socquet, and C. Vigny (2012), Interseismic coupling, segmentation and mechanical behavior of the central Chile subduction zone, *J. Geophys. Res.*, **117**, B03406, doi:10.1029/2011JB008736.
- Métois, M., A. Socquet, C. Vigny, D. Carrizo, S. Peyrat, A. Delorme, E. Maureira, M.-C. Valderas-Bermejo, and I. Ortega (2013), Revisiting the North Chile seismic gap segmentation using GPS-derived interseismic coupling, *Geophys. J. Int.*, **194**(3), 1283–1294, doi:10.1093/gji/ggt183.
- Moreno, M., M. Rosenau, and O. Oncken (2010), 2010 Maule earthquake slip correlates with pre-seismic locking of Andean subduction zone, *Nature*, **467**(7312), 198–202, doi:10.1038/nature09349.
- Müller, R. D., M. Sdrolias, C. Gaina, and W. R. Roest (2008), Age, spreading rates, and spreading asymmetry of the world's ocean crust, *Geochem. Geophys. Geosyst.*, **9**, Q04006, doi:10.1029/2007GC001743.
- Nishenko, S. P. (1991), Circum-Pacific seismic potential, U.S. Geological Survey, National Earthquake Information Center.
- Nocquet, J.-M., E. Calais, Z. Altamimi, P. Sillard, and C. Boucher (2001), Intraplate deformation in western Europe deduced from an analysis of the International Terrestrial Reference Frame 1997 (ITRF97) velocity field, *J. Geophys. Res.*, **106**, 11,239–11,257, doi:10.1029/2000JB900410.
- Nocquet, J.-M., et al. (2014), Motion of continental slivers and creeping subduction in the northern Andes, *Nat. Geosci.*, **7**(March), 287–291, doi:10.1038/NGEO2099.
- Norabuena, E. O., L. Leffler-griffin, A. Mao, T. Dixon, S. Stein, I. S. Sacks, L. Ocola, and M. Ellis (1998), Space geodetic observations of Nazca-South America convergence across the central Andes, *Science*, **279**(5349), 358–362, doi:10.1126/science.279.5349.358.
- Oleskevich, D. A., R. D. Hyndman, and K. Wang (1999), The updip and downdip limits to great subduction earthquakes: Thermal and structural models of Cascadia, south Alaska, SW Japan, and Chile, *J. Geophys. Res.*, **104**, 14,965–14,991, doi:10.1029/1999JB900060.
- Oncken, O., D. Hindle, J. Kley, K. Elger, P. Victor, and K. Schemmann (2006), Deformation of the central Andean upper plate system—Facts, fiction, and constraints for plateau models, in *The Andes*, edited by O. Oncken et al., pp. 3–27, Springer, Heidelberg, Germany.
- Pelayo, A. M., and D. A. Wiens (1990), The November 20, 1960 Peru tsunami earthquake: Source mechanism of a slow event, *Geophys. Res. Lett.*, **17**, 661–664, doi:10.1029/GL017i006p00661.
- Perfettini, H., et al. (2010), Seismic and aseismic slip on the central Peru megathrust, *Nature*, **465**(7294), 78–81, doi:10.1038/nature09062.
- Pritchard, M. E., E. O. Norabuena, C. Ji, R. Boroschek, D. Comte, M. Simons, T. H. Dixon, and P. A. Rosen (2007), Geodetic, teleseismic, and strong motion constraints on slip from recent southern Peru subduction zone earthquakes, *J. Geophys. Res.*, **112**, B03307, doi:10.1029/2006JB004294.
- Robinson, D., P. S. Das, and A. Watts (2006), Earthquake rupture stalled by a subducting fracture zone, *Science*, **312**(5777), 1203–5, doi:10.1126/science.1125771.
- Rochat, P., G. Héral, P. Baby, G. Mascle, and O. Aranibar (1998), Analyse géométrique et modèle tectonosédimentaire de l'Altiplano nord Boliviens, *Tectonics*, **32**, 769–775.
- Rodríguez Mejía, R. (2008), El sistema de fallas Chonta y sus implicancias Metalogenéticas entre 12°15'S y 13°30'S (Huancavelica-Perú), Universidad Politécnica de Madrid. MSc. thesis (2008), 116p.
- Rothman, D. (1986), Automatic estimation of large residual statics corrections, *Geophysics*, **51**(2), 332–346.
- Royden, L. H. (1993), The steady state thermal structure of eroding orogenic belts and accretionary prisms, *J. Geophys. Res.*, **98**, 4487–4507, doi:10.1029/92JB01954.
- Ruiz, S., M. Métois, A. Fuenzalida, J. Ruiz, F. Leyton, R. Grandin, C. Vigny, R. Madariaga, and J. Campos (2014), Intense foreshocks and a slow slip event preceded the 2014 Iquique M_w 8.1 earthquake, *Science*, **345**, 1165–1169.
- Salichon, J., B. Delouis, P. Lundgren, D. Giardini, M. Costantini, and P. Rosen (2003), Joint inversion of broadband teleseismic and interferometric synthetic aperture radar (InSAR) data for the slip history of the M_w = 7.7, Nazca Ridge (Peru) earthquake of 12 November 1996, *J. Geophys. Res.*, **108**(B2), 2085, doi:10.1029/2001JB000913.
- Savage, J. C. (1983), A dislocation model of strain accumulation and release at a subduction zone, *J. Geophys. Res.*, **88**, 4984–4996, doi:10.1029/JB088iB06p04984.
- Scherrenberg, A. F., R. J. Holcombe, and G. Rosenbaum (2014), The persistence and role of basin structures on the 3D architecture of the Marañón Fold-Thrust Belt, Peru, *J. South Am. Earth Sci.*, **51**, 45–58.
- Schurr, B., et al. (2014), Gradual unlocking of plate boundary controlled initiation of the 2014 Iquique earthquake, *Nature*, **512**(7514), 299–302, doi:10.1038/nature13681.
- Seiner Lizárraga, L. (2009), in *Historia de los sismos en el Perú. Catálogo: Siglos XV-XVII*, edited by F. Editorial, Univ. de Lima, Lima.
- Sempere, T., et al. (2004), Sistemas transcurrentes de escala litosférica en el sur del perú, in *Nuevas contribuciones del IRD y sus contrapartes al conocimiento geológico del sur del Perú*, Publicación Espec. Bol. la Soc. Geológica del Perú, vol. 5, edited by J. Jacay and T. Sempere, pp. 105–110, Boletín. Soc. Geológica del Perú, Lima.
- Sen, M., and P. Stoffa (1991), Nonlinear one-dimensional seismic waveform inversion using simulated annealing, *Geophysics*, **56**(10), 1624–1638.
- Silgado, E. (1978), *Historia de los sismos más notables ocurridos en el Perú (1513–1974)*, Geodinámica e Ingeniería Geológica, Serie C., vol. 3, edited by I. G. y Minería, Instituto de Geología y Minería, Perú, Lima.
- Sladen, A., H. Tavera, M. Simons, J. P. Avouac, A. O. Konca, H. Perfettini, L. Audin, E. J. Fielding, F. Ortega, and R. Cavagnoud (2010), Source model of the 2007 M_w 8.0 Pisco, Peru earthquake: Implications for seismogenic behavior of subduction megathrusts, *J. Geophys. Res.*, **115**, B22405, doi:10.1029/2009JB006429.

- Soloviev, S. L., and C. N. Go (1975), A catalogue of tsunamis on the eastern shore of the Pacific Ocean, Moscow, "Nauka" Publishing House, 202p. English translation: Soloviev S.L., Go Ch.N. (1984). *A catalogue of tsunamis on the eastern shore of the Pacific ocean, Translation by Canada Instit*, Ottawa, Canada KIA 0S2.
- Sparkes, R., F. Tilmann, N. Hovius, and J. Hillier (2010), Subducted seafloor relief stops rupture in South American great earthquakes: Implications for rupture behaviour in the 2010 Maule, Chile earthquake, *Earth Planet. Sci. Lett.*, 298, 89–94, doi:10.1016/j.epsl.2010.07.029.
- Spiske, M., J. Piepenbreier, C. Benavente, A. Kunz, H. Bahlburg, and J. Steffahn (2013), Historical tsunami deposits in Peru: Sedimentology, inverse modeling and optically stimulated luminescence dating, *Quat. Int.*, 305, 31–44, doi:10.1016/j.quaint.2013.02.010.
- Suarez, G., P. Molnar, B. C. Burchfiel, and G. Suárez (1983), Seismicity, fault plane solutions, depth of faulting, and active tectonics of the Andes of Peru, Ecuador, and southern Colombia, *J. Geophys. Res.*, 88, 10,403–10,428, doi:10.1029/JB088iB12p10403.
- Tarantola, A. (2005), Inverse problem theory and methods for model parameter estimation, 2005th ed., SIAM, Society for Industrial and Applied Mathematics, Paris.
- Tavera, H., and E. Buforn (1998), Sismicidad y sismotectónica del Perú, *Fis. la Tierra*, 10, 187–219.
- Tran, D. T. (2013), Analyse rapide et robuste des solutions GPS pour la Tectonique, Université de Nice Sophia Antipolis, France, PhD diss. 154p.
- Turcotte, D. L., and G. Schubert (2002), *Geodynamics*, 2nd ed., Cambridge Univ. Press, Cambridge/New York.
- Valladares, C. E., and J. L. Chau (2012), The Low-Latitude Ionosphere Sensor Network (LISN): Initial results, *Radio Sci.*, 47, RS0L17, doi:10.1029/2011RS004978.
- Veloza, G., R. Styron, M. Taylor, and A. Mora (2011), Open-source archive of active faults for northwest South America, *Gsa Today*, 22(10), 4–10, doi:10.1130/GSAT-G156A.1.
- Villegas-Lanza, J. C., J.-M. Nocquet, F. Rolandone, M. Vallée, H. Tavera, F. Bondoux, T. Tran, X. Martin, and M. Chlieh (2016), A mixed seismic-aseismic stress release episode in the Andean subduction zone, *Nat. Geosci.*, 9(2), 150–154, doi:10.1038/NGEO2620.
- Wang, K., and S. L. Bilek (2014), Invited review paper: Fault creep caused by subduction of rough seafloor relief, *Tectonophysics*, 610, 1–24, doi:10.1016/j.tecto.2013.11.024.
- Wang, K., Y. Hu, M. Bevis, E. Kendrick, R. Smalley, R. Barriga, and E. Lauria (2007), Crustal motion in the zone of the 1960 Chile earthquake: Detangling earthquake-cycle deformation and forearc-slier translation, *Geochem. Geophys. Geosyst.*, 8, Q10010, doi:10.1029/2007GC001721.
- Watts, A., A. Koppers, and D. Robinson (2010), Seamount subduction and earthquakes, *Oceanography*, 23(1), 166–173, doi:10.5670/oceanog.2010.68.
- Wells, D., and K. Coppersmith (1994), New empirical relationships among magnitude, rupture length, rupture width, rupture area, and surface displacement, *Bull. Seismol. Soc. Am.*, 84(4), 974–1002.
- Wessel, P., and W. H. F. Smith (1998), New, improved version of generic mapping tools released, *Eos Trans. AGU*, 79(47), 579–579, doi:10.1029/98EO00426.